J. Fluid Mech. (2026), *vol.* 1040, A47, doi:10.1017/jfm.2026.11896

Energy dissipation mechanisms in an acoustically driven slit

Haocheng Yu[1,2,*], **Tianyi Chu**[2,*] **and Spencer H. Bryngelson**[1,2,3]

[1]Daniel Guggenheim School of Aerospace Engineering, Georgia Institute of Technology, Atlanta, GA 30332, USA

[2]School of Computational Science & Engineering, Georgia Institute of Technology, Atlanta, GA 30332, USA

[3]George W. Woodruff School of Mechanical Engineering, Georgia Institute of Technology, Atlanta, GA 30332, USA

Corresponding authors: Tianyi Chu, tchu72@gatech.edu; Haocheng Yu, haochey@gatech.edu

(Received 23 December 2025 UTC; revised 21 June 2026 UTC; accepted 5 July 2026 UTC)

We quantify the conversion of incident acoustic energy into vortical motion and viscous dissipation for a plane wave passing through large-aspect-ratio slit geometries. We perform direct numerical simulations over a broad imposed parameter space in incident sound pressure level (ISPL), Strouhal number (*St*) and Reynolds number (*Re*). Spectral proper orthogonal decomposition yields energy-ranked coherent structures at each frequency, from which we construct mode-by-mode fields for spectral kinetic energy (KE) and viscous loss (VL) to examine the acoustic absorption mechanisms. At $ISPL = 150\,\mathrm{dB}$, the acoustic–hydrodynamic energy conversion is highest when $St \le 4St_0$, corresponding to an effective Keulegan–Carpenter number (K_c) larger than 40. In this regime, three-dimensional simulations show that the dominant flow response is two-dimensional, with the oscillatory shear layer near the slit corners rolling up into shedding vortices. The VL accounts for 20 %–60 % of the KE contribution. For larger *St*, the Stokes-layer confinement produces X-shaped near-slit modes, reducing the energy input by approximately 50 %. The influence of *Re* depends on amplitude. Larger *Re* corresponds to suppressed broadband fluctuations and sharpened harmonic peaks at 150 dB. At $ISPL = 120\,\mathrm{dB}$, the boundary layers remain attached, vortex shedding is weak, absorption monotonically scales with viscosity and the *Re*- and *St*-dependencies become comparable. Across all conditions, more than 99 % of the VL is confined to a compact region

[*]Equal contribution.
Code available at: https://github.com/MFlowCode/MFC.

surrounding the slit mouth. The KE–VL spectra identify regimes that enhance or suppress acoustic damping in slit geometries, providing a physically interpretable basis for acoustic-based design.

Key words: vortex shedding, acoustics, boundary layers

1. Introduction

The interaction between acoustic waves and fluid flows in confined geometries is a fundamental topic in fluid mechanics, with significant implications for acoustic damping, noise control and the design of acoustic liners. Slit resonators, characterised by narrow openings in rigid boundaries, serve as canonical models for studying such interactions due to their simplicity and the richness of the underlying physics. The vortices shed in these systems can exhibit an irregular dynamics, despite the associated velocity fluctuations remaining small and the acoustically induced flow typically operating at low Mach and Reynolds numbers. These systems exhibit complex behaviours from the coupling between incident acoustic waves and the generation of vortical structures, leading to energy conversion and dissipation mechanisms that are not fully understood. The canonical configuration, an infinitely long slit cut into a rigid plate and terminated by a deep backing cavity, was first analysed by Ingard (1953) and later revisited (Tam & Kurbatskii 2000; Tam *et al.* 2001, 2005, 2008). However, the damping of acoustic waves from their propagation through the slit, separate from the resonant response of the backing cavity, is usually considered only implicitly and has rarely been investigated as an isolated mechanism. In many practical devices (e.g. aeroengine liner, automotive mufflers and heating, ventilation and air conditioning silencers), the backing cavity tunes the global resonant response through reactive loading, thereby shifting the frequency band of strong absorption and altering the local pressure and velocity at the slit. The present study, therefore, does not seek to predict the tuned performance of a particular slit–cavity configuration, but instead focuses on the dissipation mechanisms localised at the slit mouth. To this end, we consider a cavity-free slit with anechoic termination.

Three non-dimensional parameters characterise the acoustic source and the surrounding medium and play central roles in the engineering design of narrow slits, leaks and small apertures: the acoustic amplitude, characterised by the incident sound pressure level (ISPL); the acoustic frequency, characterised by the Strouhal number (*St*); and the viscous effects, characterised by the Reynolds number (*Re*). These effects are important in applications such as acoustic liners in jet engines, ocean sonars, hearing protection devices and small structural gaps in transportation and aerospace systems; see the schematic in figure 1(*a*). Depending on the application and the surrounding medium, one may seek either to attenuate the incident acoustic waves or to preserve them. The present simulations are performed in the absence of any bias or grazing flow across the slit, and are driven purely acoustically. Our results therefore apply directly only to conditions without bias and grazing flow.

In the low-amplitude, low-frequency regime, the dissipative behaviour of a slit can be predicted reasonably well by linearised boundary-layer theory, which attributes losses to viscous diffusion within the Stokes layer adjacent to the walls. Abily *et al.* (2023) recently demonstrated that a transfer-matrix-method-based analytical model accurately predicts the sound absorption observed experimentally for amplitudes below 120 dB and frequencies below 2 kHz. In parallel, Qu *et al.* (2023) and Hoppen *et al.* (2023) proposed analytical models for Helmholtz resonators that remain in good agreement with both simulations and experiments up to 140 dB. For higher forcing levels, the flow inside the slit develops into a vortex roll-up, skew-symmetric jetting and, eventually, vortex shedding from the slit exit. These effects emerge when the acoustic frequency and amplitude yield a Stokes boundary-layer thickness comparable to the slit height, or when the acoustic particle displacement exceeds the slit thickness, corresponding to a Keulegan–Carpenter number K_c of order unity or greater. In this regime, the kinetic energy of the induced vortices, together with their viscous dissipation, becomes the primary mechanism of acoustic energy losses (Howe 1980; Cummings 1984; Tam *et al.* 2001). Such nonlinear phenomena can alter the acoustic resistance of slit-based resonant elements relative to linear predictions (Tam *et al.* 2001, 2005), and present uncertainty for designers.

Different slit and flow configurations can give rise to a qualitatively different vortex dynamics. In two-dimensional (2-D) slit resonators with grazing flow, numerical studies have suggested possible interactions between neighbouring resonators, because shed vortices may penetrate the boundary layer (Tam *et al.* 2008; Zhang & Bodony 2011). When three-dimensional (3-D) effects are included, vortex rings may develop in rectangular resonator configurations of small aspect ratio (Tam *et al.* 2010; Qiang *et al.* 2022), and become line vortices at large aspect ratios (Tam *et al.* 2010; Xu *et al.* 2014). Xu *et al.* (2014) further showed that, at 150 dB, the absorption coefficients from 2-D simulations can accurately approximate those from 3-D simulations. Later, Zhang & Bodony (2016) showed numerically that grazing turbulent boundary-layer flow can also suppress the formation of vortex rings in honeycomb resonators.

In the present work, we focus on a cavity-free slit in the large-aspect-ratio limit. The background flow is quiescent, so there is no natural velocity scale associated with a base flow through the slit. We therefore organise the study primarily in terms of imposed operating conditions, prescribed directly by the fluid properties, geometry and acoustic source, while also reporting the corresponding induced in-slit parameters that characterise the realised flow response. We construct a database using direct numerical simulations (DNSs) to characterise the dependence on the imposed Reynolds number, Strouhal number and ISPL, and to establish the mapping between these imposed parameters and the induced in-slit flow parameters that govern the local dynamics. Complementary 3-D simulations at an aspect ratio of 22 show only weak spanwise variation, indicating that the dominant flow dynamics remains effectively two-dimensional. The present database is suitable for examining the onset and scaling of sound-induced vortex shedding, the spatial structure of kinetic-energy-dominant and viscous-loss-dominant components and the role of nonlinear acoustic response in narrow-slit geometries. We use this database to quantify the acoustic damping under each imposed operating condition and to clarify the underlying dissipation mechanisms of plane acoustic waves as they propagate through the slit.

While the existence of vortex-based energy conversion in slit resonators has been well examined using probes, fundamental scientific questions of engineering relevance remain open. The *St*-dependence remains to be characterised. Although empirical evidence indicates that the interaction between the oscillating boundary layer and the bulk flow is strongest when *St* is $O(1)$ (Tam *et al.* 2005, 2008; Chen & Li 2020; Aulitto *et al.* 2022), the scaling of modal energy across different spectral components with *St* has not been quantified. Amplitude dependence also requires further clarification. Most available measurements collapse acoustic amplitude into a single non-dimensional excursion parameter, such as absorption coefficient and acoustic impedance (Chung & Blaser 1980; Tam *et al.* 2001, 2005; Abily *et al.* 2023); however, this practice can mask the cascade of triadic interactions that emerges once the particle displacement exceeds roughly 10 % of the slit height. In addition, the *Re*-dependence is not fully resolved. At fixed acoustic amplitude, increased Reynolds number in irregular regimes expands the inertia-dominated near-wall region and promotes earlier shear-layer roll-up near the slit inlet (Abily *et al.* 2023). The interaction of this shift with amplitude-induced vortex breakdown remains unclear, yet it influences the high-frequency performance limits of practical resonator designs. To examine the energy dissipation mechanisms across these parameter variations, modal-decomposition techniques provide a framework for quantifying the contributions of coherent flow structures across different scales.

Our goal is to disentangle the contributions of the acoustic component, quantified by scalar pressure fluctuations, from the kinetic energy (KE) component of the induced flow field, from the vortex dynamics, together with the overall viscous dissipation, which we refer to as the viscous-loss (VL) component. Proper orthogonal decomposition (POD) provides an efficient statistical way to extract energy-ranked spatial structures from flow-field data (Lumley 1967, 1970). In practice, POD uses the method of snapshots, which involves the eigendecomposition of the spatial cross-correlation tensor (Sirovich 1987). In the context of acoustic slits, POD has been applied to phase-locked particle image velocimetry measurements of a dual-slit cavity, where the most energetic modes exhibit pronounced asymmetry (Tang *et al.* 2025). In general, the POD modes do not distinguish between hydrodynamic and acoustic components, as the method lacks scale separation in frequency (Berkooz *et al.* 1993). Dynamic mode decomposition (DMD) addresses part of this limitation by providing a spatio-temporal decomposition of time-resolved data streams, associating each mode with a single complex frequency and its corresponding growth/decay rate (Schmid 2010). Using DMD on DNS data of the transient vortex dynamics in an acoustic-driven slit, Qiang *et al.* (2022) showed that the most dominant dynamical structures also exhibit asymmetry perpendicular to the direction of sound propagation. Nonetheless, DMD can be sensitive to subsampling and may struggle to converge in statistically stationary turbulent flows, typically requiring carefully designed ensemble-based formulations.

As an alternative to the above data-driven modal-decomposition techniques, spectral POD (SPOD) operates analogously to POD but in the frequency domain, enabling the identification of energy-ranked structures that evolve coherently in both space and time (Schmidt *et al.* 2018; Towne *et al.* 2018). The SPOD modes represent both the statistical and dynamical contents of the flow at each frequency, optimally representing second-order statistics and serving as optimally averaged ensemble DMD modes (Towne *et al.* 2018). Readers are referred to Schmidt & Colonius (2020) for the practical implementation of SPOD. Spectral proper orthogonal decomposition has been widely applied to extract both coherent acoustic and hydrodynamic structures in various turbulent flows, including cylinders (Awasthi *et al.* 2025), airfoil wakes (Sano *et al.* 2019; Himeno *et al.* 2021) and jets (Schmidt *et al.* 2018; Nekkanti & Schmidt 2021*a*; Nogueira *et al.* 2022; Bugeat *et al.* 2024). In these contexts, SPOD isolates dominant spectral flow features, such as vortex-shedding modes in resonators. It provides a natural way to analyse their associated linear mechanisms, including advection, production and dissipation. Recently, Tang *et al.* (2023) proposed an SPOD-based noise-reduction strategy to improve the performance of acoustic liners in a steam turbine control valve using 3-D delayed detached eddy simulation. Recent work has also compared SPOD with other modal-decomposition approaches for separating acoustic and hydrodynamic fluctuations in liner flows (e.g. Scarano *et al.* 2026), highlighting the utility of frequency-resolved coherent structures in aeroacoustic configurations. In this work, we use SPOD to separate and quantify the mode-by-mode, frequency-resolved KE and VL components and their spatial structures, providing explicit modal–spectral energetics in a slit-mouth configuration. Figure 1(*b*) shows a schematic of how the total damping of the incident acoustic energy within a

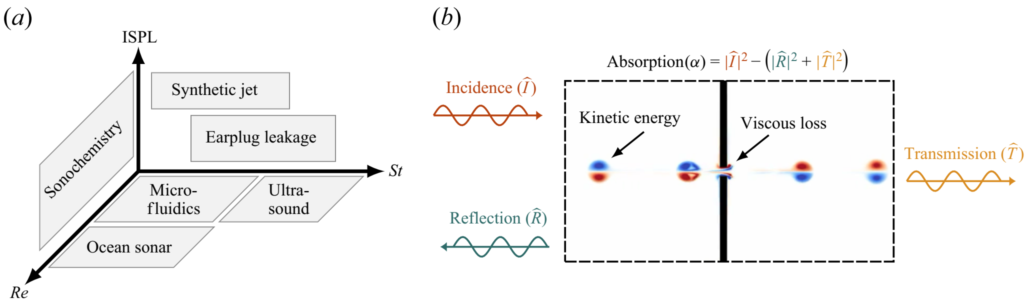

Figure 1. Schematics of (*a*) the parameter space explored in this study and (*b*) the global energy pathways, showing the conversion of incident acoustic energy into the kinetic energy of shed vortices and its subsequent viscous dissipation. The indicative regions for representative applications in (*a*) are order-of-magnitude estimates and are intended to convey relative placement rather than strict bounds.

control volume is distributed among different spectral KE and VL components. The resulting spectral KE and VL fields exhibit localised structures within and near the slit, through which we reveal the acoustic–KE–VL energy-exchange mechanism at the slit mouth as a coupled effect of *St*, *Re* and ISPL. By spatially and spectrally integrating these fields, we recover conventional global measures of acoustic power loss inferred from reflection and transmission, thereby linking the underlying modal energetics to the net absorption.

This paper is outlined as follows. In § 2, we introduce the high-fidelity numerical approach for a plane wave traversing a slit mouth. In § 3, we detail the resulting database and characterise the in-slit flow parameters induced by the imposed operating conditions. In § 4, we use SPOD-based spectral analysis to quantify the dissipation mechanisms associated with each spectral KE and VL component and demonstrate how variations in *St*, *Re* and ISPL affect the energy transfer from acoustic waves to vortical structures. Our results reveal the acoustic–KE–VL energy-exchange mechanism at the slit mouth, its dependence on the governing parameters and its connection to the boundary-layer absorption. The trend of the volume-integrated SPOD-based dissipation $\mathcal{P}$ is consistent with the acoustic absorption coefficient obtained from the three-microphone method, confirming that the spectral decomposition captures the dominant dissipation mechanisms. Future work can focus on a fully closed power balance matching $\mathcal{P}$ to the absorption coefficient, by extending the domain of SPOD analysis to include all boundary flux terms. Sections 5 and 6 summarise the main contributions and discuss limitations and implications for acoustic slit design.

2. Direct numerical simulation

Throughout this work, we adopt the following notational convention: scalar-valued functions are denoted by italicised symbols (e.g. q); vector-valued functions by bold italic symbols (e.g. $\boldsymbol{q}$). Spatially discretised quantities are denoted with vector notation, discretised scalars $\boldsymbol{q}$ and discretised vectors as q.

2.1. *Governing equations and numerical method*

To represent the propagation of sound waves through slits, the flow motion is modelled using the compressible Navier–Stokes equations, encompassing the continuity, momentum and energy equations

$$\frac{\partial \rho}{\partial t} + \nabla \cdot (\rho \boldsymbol{u}) = h_s h_\delta / c, \tag{2.1}$$

$$\frac{\partial}{\partial t}(\rho \boldsymbol{u}) + \nabla \cdot (\rho \boldsymbol{u}\boldsymbol{u}^\mathsf{T}) + \nabla p - \nabla \cdot \boldsymbol{T} = h_s h_\delta \boldsymbol{n}, \tag{2.2}$$

$$\frac{\partial}{\partial t}(\rho E) + \nabla \cdot \left[(\rho E + p)\boldsymbol{u} - \boldsymbol{T} \cdot \boldsymbol{u}\right] = 0, \tag{2.3}$$

where $\boldsymbol{u} = [u,\ v]^\mathsf{T}$ is the velocity vector field, c is the speed of sound, ρ is the density, p is the pressure, and E is the total energy, $\boldsymbol{n}$ is the unit vector directed from the sound source toward the slit and

$$\boldsymbol{T} \equiv \frac{1}{Re}\left[\nabla \boldsymbol{u} + (\nabla \boldsymbol{u})^\mathsf{T} - \frac{2}{3}(\nabla \cdot \boldsymbol{u})\, \boldsymbol{I}\right] \tag{2.4}$$

is the viscous stress tensor, with the bulk viscosity assumed negligible and thus omitted. The one-way plane wave source is modelled using two non-conservative source terms (Maeda & Colonius 2017), where h_s is the time-dependent amplitude of the monopole and dipole sources, and h_δ represents the Gaussian monopole support function provided by Maeda & Colonius (2017). The source terms in (2.1) and (2.2) represent a planar monopole and dipole source, respectively. The source terms cancel each other in one direction, resulting in a one-way planar sound source. All sound waves are assumed to be harmonic, implying that the time-dependent amplitude

$$h_s = \widehat{A}\sin(2\pi f_s t), \tag{2.5}$$

is sinusoidal with time, where $\widehat{A}$ is the pressure amplitude and $2\pi f_s$ is the angular frequency of the sound source. Closure is achieved using the ideal gas equation of state

$$p = (\gamma - 1)\, \rho e, \tag{2.6}$$

which relates the internal energy, e, to the total energy of the fluid, $E = e + \|\boldsymbol{u}\|^2/2$. Here, $\gamma = 1.4$ is the ratio of specific heats. Equations (2.1)–(2.6) are non-dimensionalised by the speed of sound, $c = 343\ \mathrm{m\ s^{-1}}$ and the slit opening, o, and thickness, $d = o = 0.8$ mm, and are parameterised by the Strouhal number $St = 2\pi f_s o/c$ and the Reynolds number $Re = \rho c o/\mu$. Here, ρ is the density of air and μ is the dynamic viscosity, which varies with the Reynolds number across different simulations. The nominal Strouhal number and Reynolds number are defined as $St_0 = 2\pi f_{s,0} o/c$ and $Re_0 = \rho_0 c o/\mu_0$, respectively, where $f_{s,0} = 0.5$ kHz is the reference frequency. The reference density and dynamic viscosity are taken as near-sea-level air properties, $\rho_0 = 1.19\ \mathrm{kg\ m^{-3}}$ and $\mu_0 = 1.84 \times 10^{-5}\mathrm{Pa\ s}$, respectively. All the length scales, x, are non-dimensionalised by d, time t by c/d, velocity u by c, pressure p by $\rho_0 c^2$, the source terms in the (2.1) $h_s h_\delta/c$ by $d/\rho_0 c$ and source terms in the (2.2) $h_s h_\delta \boldsymbol{n}$ by $d/\rho_0 c^2$.

We perform DNSs using MFC, a GPU-accelerated compressible flow solver (Bryngelson *et al.* 2021; Radhakrishnan *et al.* 2024; Wilfong *et al.* 2025*a*,*b*,*c*). Equations (2.1)–(2.4) can be written compactly as

$$\frac{\partial \boldsymbol{q}}{\partial t} + \nabla \cdot \boldsymbol{F}(\boldsymbol{q}) = \boldsymbol{s}(\boldsymbol{q}), \tag{2.7}$$

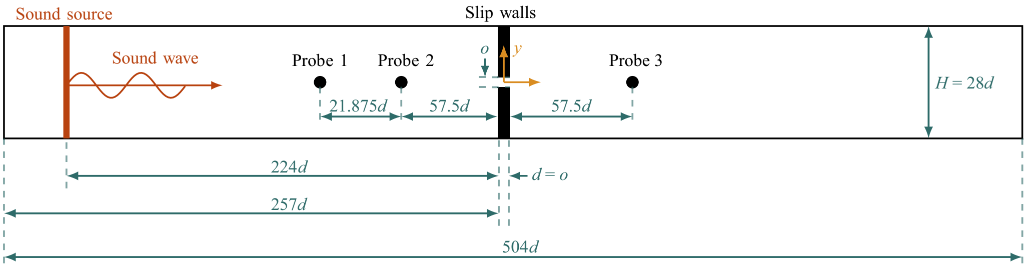

Figure 2. Schematic of the flow configuration in the x–y domain simulated in this work.

where

$$\boldsymbol{q} = \begin{bmatrix} \rho \\ \rho \boldsymbol{u} \\ \rho E \end{bmatrix}, \quad \boldsymbol{F} = \begin{bmatrix} \rho \boldsymbol{u} \\ \rho \boldsymbol{u} \otimes \boldsymbol{u} + p\boldsymbol{I} - \boldsymbol{T} \\ (\rho E + p)\boldsymbol{u} - \boldsymbol{T} \boldsymbol{\cdot} \boldsymbol{u} \end{bmatrix} \quad \text{and} \quad \boldsymbol{s} = \begin{bmatrix} h_s h_\delta / c \\ h_s h_\delta \boldsymbol{n} \\ 0 \end{bmatrix}, \tag{2.8}$$

represent the state vector, flux tensor and the source vector, respectively. The spatial discretisation of (2.7) and (2.8) uses a finite-volume method, which is well suited to problems involving irregular geometries and complex compressible flows. A fifth-order accurate weighted essentially non-oscillatory scheme (Coralic & Colonius 2014) is used to reconstruct the fluxes and viscous terms, which handles sharp gradients in the high-amplitude solution without introducing spurious oscillations. We perform temporal discretisation using a total variation diminishing third-order accurate Runge–Kutta scheme (Gottlieb & Shu 1998).

2.2. *Simulation configurations*

Figure 2 shows the configuration of the 2-D computational domain, $\varOmega$, discretised with a uniformly structured mesh with equal grid spacing. Rightward-going acoustic waves were emitted from a planar acoustic source 224d from the incident face of the slit resonator (28d away from the left domain boundary), where $d = 0.8$ mm. The domain height is H, where $H = 28\,d$. Ghost-cell non-reflective boundary conditions are used on the left and right boundaries, where primitive variables in the ghost cells are extrapolated from the interior to satisfy $\partial(\boldsymbol{\cdot})/\partial n \approx 0$, and n represents the direction perpendicular to the boundary. In practical systems, the boundary layers at the top and bottom domain walls may contribute to overall absorption. However, the present simulations intentionally isolate the dissipation associated with the slit mouth itself, so we neglected dissipation due to sound at the top and bottom domain boundaries and treated these surfaces as characteristic slip walls, following Thompson (1990). The no-slip condition was enforced on the incident face of the slit and on all of its interior walls using the immersed-boundary method (Tseng & Ferziger 2003). Since heat conduction is not included in the governing equations, no thermal boundary condition is prescribed at the solid walls. The temperature field is obtained diagnostically from the equation of state using the local thermodynamic variables, and the immersed-boundary treatment therefore only enforces the velocity, pressure and density boundary conditions at the walls.

The immersed-boundary treatment uses ghost cells on a Cartesian finite-volume mesh. The boundary condition is enforced through an image-point reconstruction in which the flow variables at each ghost cell are interpolated between the body-intercept point on the immersed surface and a corresponding image point in the fluid domain, consistent with the ghost-cell immersed-boundary methodologies (Tseng & Ferziger 2003; Mittal & Seo

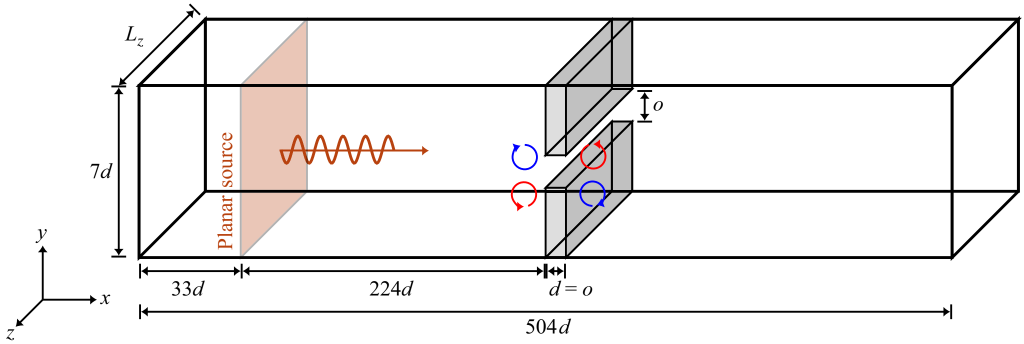

Figure 3. Schematic of the 3-D simulation configuration. The slit is embedded in an x–y domain and extended uniformly in the spanwise direction z with periodic boundary conditions. A spanwise-uniform acoustic source drives the flow. Two spanwise extents are considered, $L_{z,1} = 11d$ and $L_{z,2} = 22d$. All other parameters are identical. The companion 2-D simulation in figure 2 uses the identical x–y configuration.

2023). This reconstruction involves a second-order interpolation, so the formal accuracy of the boundary closure is second order, even though the underlying finite-volume discretisation retains its high-order accuracy away from the immersed surface.

We use the ISPL to represent the decibel sound level at a specific frequency, defined as

$$ISPL = 20 \log_{10} \left(\widehat{p}/\widehat{p}_{ref}\right), \tag{2.9}$$

where $\widehat{p} = \widehat{A}/\sqrt{2}$ is the dimensional root-mean-squared pressure of the sound, and $\widehat{p}_{ref} = 20\ \mu$ Pa is the standard reference pressure in air.

The 2-D slit under consideration is a wall-bounded problem, and the oscillatory boundary layer is a near-wall feature characterised by steep gradients, rather than a propagating wave. Previous work has found that the acoustic-driven flow bounded by small slit resonators, as small as 1 cm, is laminar at a high incident level of 155 dB (Tam & Kurbatskii 2000). The laminar condition with an oscillatory wave gives rise to a viscous Stokes layer inside the slit opening whose thickness is much smaller than the acoustic wavelength of our range of interest (Tam *et al.* 2005, 2010). The wavelength of the oscillatory Stokes layer λ_s is defined as

$$\lambda_s \equiv 2\pi\, \delta_s = 2\sqrt{\pi\, \nu / f_s}, \tag{2.10}$$

where δ_s is the thickness of the Stokes layer, $\nu = \mu/\rho$ is the kinematic viscosity and f_s is the acoustic frequency (White 1991; Tam *et al.* 2005).

To examine the 3-D dynamics, the 2-D slit configuration in figure 2 is extended uniformly in the spanwise direction, z, with periodic boundary conditions, as shown in figure 3. The acoustic forcing is extended consistently in the spanwise direction. Two spanwise extents are considered, with $L_{z,1} = 11d$ and $L_{z,2} = 22d$. This configuration provides a more realistic setting, enabling the assessment of 3-D effects absent in 2-D simulations.

For varying acoustic frequencies, simulations are performed using at least ten cells per Stokes-layer wavelength ($\lambda_s/\Delta_x \geq 10$) to ensure negligible numerical errors when the Stokes boundary layers are resolved, where Δ_x is the grid spacing. Grid convergence is confirmed by the negligible change in simulated acoustic power absorption coefficients when the cell count is doubled. Simulations are performed over multiple acoustic cycles with a constant time step to ensure the system reaches a dynamic steady state before data collection.

Frequency (kHz)	St/St_0 (–)	Domain size ($N_x \times N_y$)	Cell size (λ_s/Δ_x)	Time step (10^4 cycle^{-1})	Duration (cycles)	Analysis range (cycles)
0.5	1	20 160 × 1120	30	8.0	25	10–25
1	2	20 160 × 1120	20	4.0	50	19–50
2	4	20 160 × 1120	15	2.0	75	12–75
3	6	20 160 × 1120	12	1.3	113	18–113
4	8	20 160 × 1120	10	1.0	150	23–150
5	10	25 200 × 1400	12	0.8	139	20–139
6	12	25 200 × 1400	10	0.7	167	24–167

Table 1. Simulation configuration of seven different acoustic frequencies. The following simulations include cases with three Reynolds numbers, $Re/Re_0 = 1$, $1/2$ and $1/3$, and two sound pressure levels: $ISPL = 120$ dB and 150 dB. The three varying parameters result in 42 unique combinations. The total number of cells in the x-direction (N_x) and the y-direction (N_y) describes the grid size of the computational domain. The number of cells per Stokes' wavelength λ_s describes the cell size. We use the number of time steps per acoustic cycle to describe the time step size.

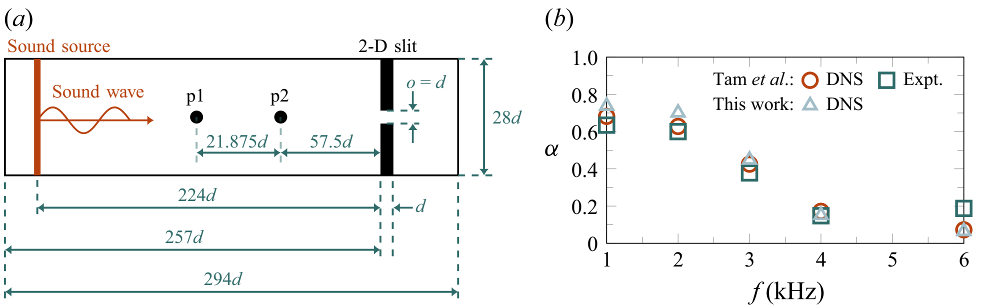

Figure 4. A 2-D slit resonator for verification showing (*a*) the computational domain with acoustic source (not to scale) and (*b*) comparison of power absorption-coefficient spectra among DNS and experiment (Expt.) of Tam *et al.* (2001) with discrete tones at $ISPL = 150$ dB.

2.3. *Direct numerical simulation verification*

We verify our numerical simulations using a 2-D simulation of a discrete tone ($ISPL = 150$ dB) propagating as a plane wave through a 2-D slit resonator. The opening, o, and thickness, d (with $o = d$), of this slit are each scaled to be $1/28$ of the domain height to reproduce the configuration of Tam *et al.* (2001). A similar verification simulation has been conducted by Yu *et al.* (2024, 2025*a*). This verification set-up is analogous to the cases examined in this study, with the computational domain having a non-dimensional length of $294d$, as illustrated in figure 4(*a*). In this verification case, we use non-reflective boundary conditions at the left horizontal boundary and impermeable slip walls for the remaining domain boundaries. The simulation time and grid size match those of the 2-D cases in table 1. Thus, the only differences between this verification simulation and the 2-D cases in table 1 are the termination boundary condition and the x-direction extent of the computational domain.

We use the power absorption coefficient as the metric to quantify the acoustic performance. The absorption coefficient that represents the percentage of the sound power dissipated by the slit resonator is defined as

$$\alpha \equiv 1 - |\widehat{R}|^2 - |\widehat{T}|^2, \tag{2.11}$$

https://doi.org/10.1017/jfm.2026.11896 Published online by Cambridge University Press

where $|\widehat{R}|^2$ and $|\widehat{T}|^2$ are the power reflection and transmission coefficients, respectively. Following Tam *et al.* (2005) and Leung *et al.* (2007), these coefficients are calculated from the recorded time histories using the transfer function method of Chung & Blaser (1980). In the present verification case with a reflective termination, all the transmitted waves will be reflected by the termination, yielding $|\widehat{T}|^2 \approx 0$. The power absorption coefficient is approximated as $\alpha \approx 1 - |\widehat{R}|^2$. For discrete-tone analysis, the power reflection coefficient at a given frequency is determined via linear interpolation between the two adjacent spectral points that bracket the target frequency.

We collect pressure data at two points along the domain's horizontal centreline at each simulation time step. The two points are $21.875d$ and $57.5d$ upstream of the slit incident face, where higher-order modes are evanescent. The sampling frequency of the recorded time history is as large as the inverse of the simulation time step. Figure 4(*b*) compares the present absorption-coefficient spectra with those reported by Tam *et al.* (2001) at a nominal incident sound intensity of 150 dB. The discrepancy between this work and Tam's DNS is within 12 % across the full frequency band, with the largest discrepancy 11.7 % occurring at 2 kHz. In Tam *et al.* (2001), KE loss is estimated by identifying and integrating the energy of individual large-scale shed vortices, and thus excludes contributions from other scales. In contrast, the absorption coefficient in the present study is obtained using the transfer-function method, which measures the net acoustic energy loss from the reflected and transmitted wave fields. Since these two approaches do not quantify the same quantity, a slight discrepancy within 12 % between the present results and those of Tam *et al.* (2001) is to be expected. Nevertheless, the overall agreement between the two DNS datasets supports the accuracy of the present numerical method for simulating slit resonators under acoustic excitation.

In the following, the MFC solver is used to generate a database for large-aspect-ratio acoustic slits over the parameter ranges detailed in § 3. The comparison between the 2-D and 3-D simulations in § 4.4 suggests that the flow remains effectively two-dimensional.

3. Database of acoustic slit

3.1. *Set-up*

The dominant factors influencing the performance of the acoustic slit include ISPL, acoustic frequency and Reynolds number. To isolate the effect of each parameter, simulations are performed across various combinations of these three variables. Specifically, two ISPLs, 120 and 150 dB, are considered to represent cases of weak and strong sound excitations, respectively. The acoustic frequency is varied from 0.5 to 6 kHz to represent a broad range of acoustic behaviours. For a fixed speed of sound and slit width, three Reynolds numbers are examined to investigate the effect of the varying dynamic viscosity. Table 1 summarises the considered parameters and the corresponding simulation configurations.

All simulations were performed using MFC on the NCSA Delta supercomputer. Each case was executed on three NVIDIA A100 GPUs. The overall GPU utilisation exceeds 90 % (Radhakrishnan *et al.* 2024). The required wall time of each simulation is approximately 40 h and depends weakly on the acoustic frequency and the corresponding grid resolution. Numerical stability is verified under a Courant–Friedrichs–Lewy number of less than 0.5. For the simulations documented in table 1, the raw data for the analysed cycles are publicly available in the Georgia Tech Digital Repository, comprising 42 MATLAB-formatted `mex` files. For each case, the full velocity and density fields are stored over the analysis range indicated in the table, comprising 640 time snapshots. The public flow-field data are down sampled by a factor of 2 in each coordinate direction. Each file is approximately 4.5 GB in size and corresponds to a unique parameter combination.

For the configurations listed in table 1, the acoustically induced flow remains at low Mach number (Ma), with $Ma \leq 0.05$ throughout the computational domain. Velocities and their fluctuations are thus small compared with the ambient speed of sound. Consequently, compressibility effects in the induced flow are weak, and the pressure fluctuations associated with acoustic propagation are only mildly affected by local density variations, which remain below 0.5 % of their initial value. This behaviour is consistent with previous studies of low-Mach-number oscillatory flows in resonant cavities, which have shown that the velocity field is predominantly solenoidal and that compressibility enters only as a higher-order correction (Landau & Lifshitz 1987). Despite the relatively low Mach numbers, the flow outside the slit exhibits a complex, irregular dynamics, whereas the flow inside the slit remains laminar. We emphasise, however, that compressibility cannot be neglected in the simulations, as compressibility is essential for accurately resolving the propagation of acoustic waves.

3.2. *Data*

To illustrate the rich physics in the database, figure 5 shows the normalised instantaneous vorticity fields

$$\boldsymbol{\omega}(\mathsf{x};\, t_i) = \frac{\left[\partial_x \boldsymbol{v} - \partial_y \boldsymbol{u}\right](\mathsf{x};\, t_i)}{\max\{\left[\partial_x \boldsymbol{v} - \partial_y \boldsymbol{u}\right](\mathsf{x};\, t_i)\}}, \tag{3.1}$$

for both 2-D and 3-D simulations at $ISPL = 150$ dB. Further 2-D results spanning a range of St–Re combinations are included in figure 30. Here, x denotes the discretised spatial coordinate vector over the computational domain. Across all cases, the snapshots reveal well-resolved boundary layers generated as the flow interacts with the slit, followed by the formation of periodic vortex shedding. These results indicate that a portion of the incident acoustic energy is converted into vortical motion through interactions with the slit. These vortical structures intensify and periodically detach from the slit, forming coherent vortices that dominate the near-slit region. Once shed, the vortices convect both upstream and downstream, undergoing complex interactions that give rise to large- and small-scale motions. As the acoustic frequency increases, the vortical structures gradually become confined to the vicinity of the slit, suppressing long-range interactions and limiting the generation of far-field vorticity. For $L_{z,1} = 11d$, hairpin-like structures emerge in the vorticity field away from the slit. For the larger spanwise extent, $L_{z,2} = 22d$, the vorticity field shows the presence of line vortices with only weak spanwise variation, indicating that the dominant flow dynamics remains effectively two-dimensional. This observation is consistent with the results of Xu *et al.* (2014) for a spanwise extent of $L_z = 40d$, where the vorticity fields likewise showed limited three-dimensionality and the absorption coefficients from 2-D and 3-D simulations were in favourable agreement. Further analysis of the present 3-D simulations is provided in § 4.4.

In the present analysis, we quantify viscous dissipation associated with these vortical structures using the irreversible viscous dissipation density $\boldsymbol{T} : \nabla \boldsymbol{u}$, which is non-negative for the Newtonian fluids we assume in this study and a measure of thermodynamic dissipation. Figure 5 further examines the instantaneous irreversible VL fields integrated

https://doi.org/10.1017/jfm.2026.11896 Published online by Cambridge University Press

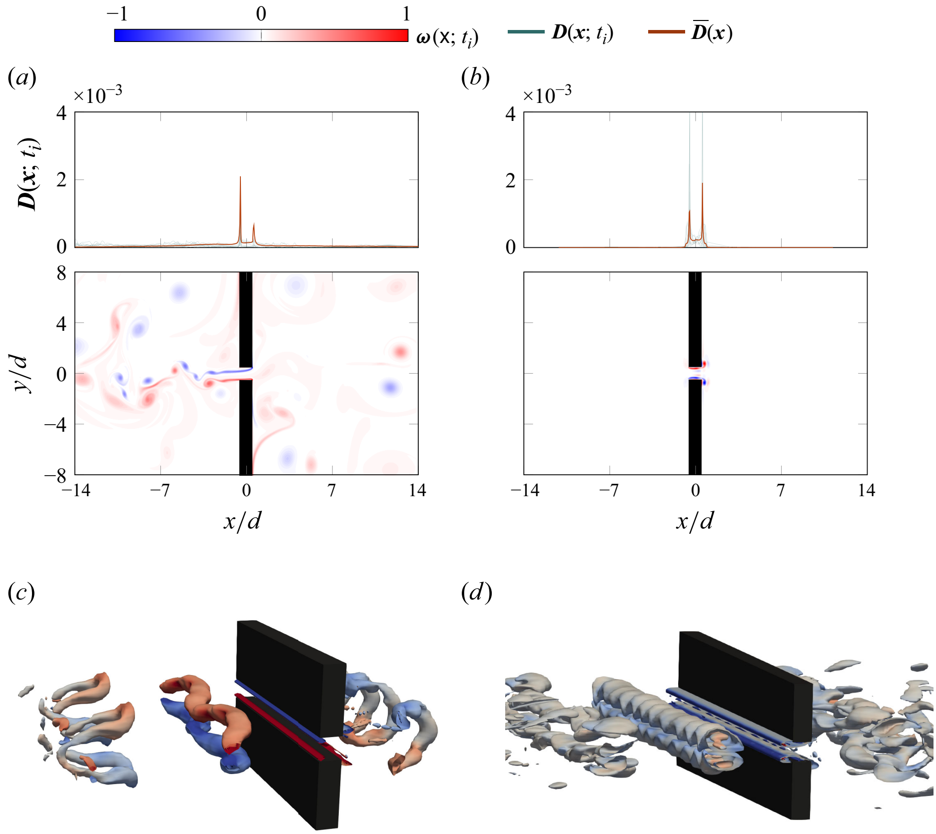

Figure 5. Instantaneous 2-D (a, b) and 3-D (c, d) vorticity fields, $\boldsymbol{\omega}(\mathsf{x};\, t_i)$, at $ISPL = 150$ dB: (a) $Re = Re_0$ and $St = St_0$; (b) $Re = Re_0/3$ and $St = 12St_0$; (c) $Re = Re_0/3$, $St = 2St_0$ and $L_{z,1} = 11d$; and (d) $Re = Re_0/3$, $St = 2St_0$ and $L_{z,2} = 22d$. The instantaneous 2-D VL fields (integrated across the y direction), $\boldsymbol{D}(\boldsymbol{x};\, t_i)$, and their temporal average, $\overline{\boldsymbol{D}}(\boldsymbol{x})$, are included in ($a$, b) for comparison. Additional 2-D results spanning a range of St–Re combinations are included in figure 30.

in the y-direction

$$\boldsymbol{D}(\boldsymbol{x};\, t_i) = \sum_{y \in [-14d, 14d]} \left[\mathsf{T} : \nabla \mathsf{u}\right](\mathsf{x};\, t_i)\,\Delta_y, \quad \text{with} \quad \mathsf{T} = \frac{1}{Re}\left(\nabla \mathsf{u} + \nabla \mathsf{u}^{\mathsf{T}} - \frac{2}{3}(\nabla \cdot \mathsf{u})\boldsymbol{I}\right), \tag{3.2}$$

where $\Delta_y = \Delta_x$ under uniform grid spacing. The corresponding temporal averages over N_t snapshots are

$$\overline{\boldsymbol{D}}(\boldsymbol{x}) = \frac{1}{N_t} \sum_{i=1}^{N_t} \boldsymbol{D}(\boldsymbol{x};\, t_i). \tag{3.3}$$

Across all cases, the VL fields peak near the slit and attain values larger than those in other regions, indicating that the dominant energy loss is associated with velocity fluctuations near the slit and their conversion into vorticity or viscous dissipation within the boundary layer. In contrast, the detached vortices contribute comparatively little. At the lower acoustic frequency of $St = St_0$, VL is larger near the inlet of the slit than at the outlet. This

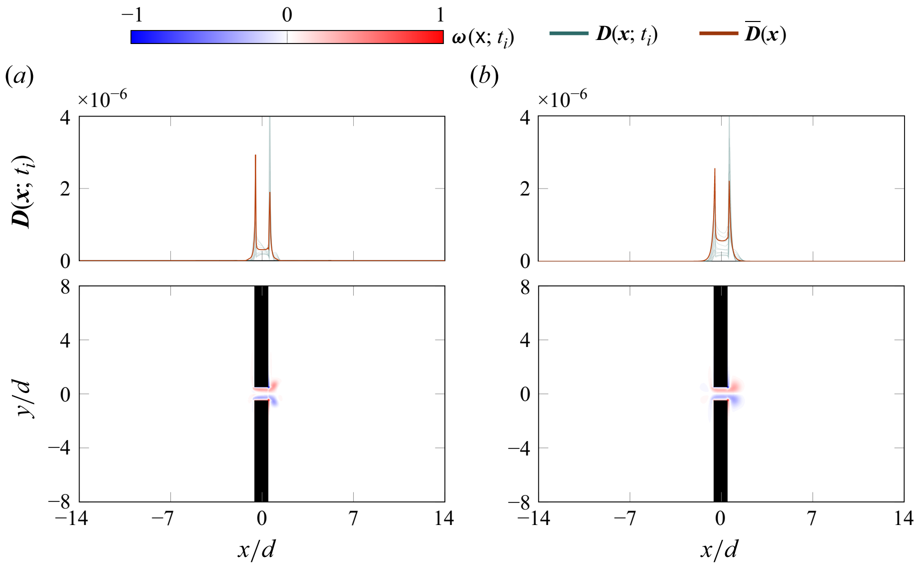

Figure 6. Instantaneous VL (integrated across the y direction), $\boldsymbol{D}(\boldsymbol{x};\,t_i)$, and vorticity fields, $\boldsymbol{\omega}(\mathrm{x};\,t_i)$, at $ISPL = 120$ dB and $St = St_0$: (*a*) $Re = Re_0$ and (*b*) $Re_0/3$.

trend is consistent with the corresponding flow fields, in which more pronounced upward-travelling vortex shedding occurs at lower frequencies. At lower Reynolds numbers within the range considered, viscous effects become more pronounced relative to inertial ones, leading to greater VL while still sustaining vortex shedding.

For comparison, figure 6 shows the results at $ISPL = 120$ dB. The flow fields with higher Strouhal numbers are similar, so we focus on a representative Strouhal number of St_0. At this weaker sound excitation, the vortex shedding remains nearly symmetric, with vorticity confined to boundary layers adjacent to the slit walls. No evidence of large-scale vortex pairing or chaotic modulation is found. Compared with high-intensity acoustic excitation, these cases exhibit substantially weaker VL, approximately 3 orders of magnitude lower.

3.3. *Mapping between imposed control parameters and induced in-slit response*

As the quiescent background flow does not provide a characteristic velocity scale for the slit flow, we distinguish between the parameters for the imposed operating condition and those induced by the resulting flow response. The imposed parameter group, (Re, St, $ISPL$), is treated as the set of controllable factors: these quantities are prescribed directly through the fluid properties, geometry and acoustic source. The in-slit shear number

$$Sh = \frac{o}{\delta_s}, \tag{3.4}$$

which measures the slit width, o, relative to the viscous boundary-layer thickness, $\delta_s = \sqrt{\mu/(\pi f_s \rho_0)}$, also depends only on the imposed configuration. By contrast, the effective in-slit Strouhal and Reynolds numbers cannot be directly specified *a priori* as the relevant in-slit velocity scale is itself an outcome of the simulation or experiment. We therefore define

$$St_{slit} = \frac{2\pi f_s o}{u_{slit,pk}}, \qquad Re_{slit} = \frac{\rho_0 u_{slit,pk}\, o}{\mu}, \tag{3.5}$$

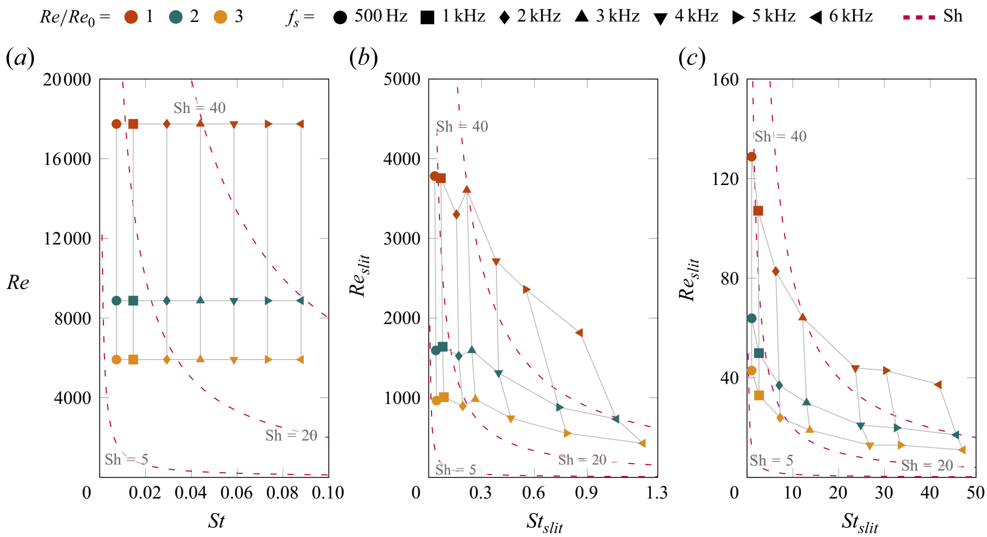

Figure 7. Mapping from the imposed dimensionless control parameters to the induced in-slit response groups: (*a*) imposed incident plane (*St*, *Re*), defined using the sound speed c_0, showing a rectangular grid formed by three viscosities, μ_0, $2\mu_0$ and $3\mu_0$ (corresponding to $Re = Re_0$, $Re_0/2$ and $Re_0/3$), and seven forcing frequencies, f_s =0.5–6 kHz; (*b*, *c*) corresponding induced response planes (St_{slit}, Re_{slit}), defined using the peak in-slit velocity, $u_{slit,pk}$, for (*b*) $ISPL = 150$ dB and (*c*) 120 dB.

based on the peak in-slit velocity

$$u_{slit,pk} \equiv \max_{t} \max_{(x,y)\in\Omega_{slit}} |u(x, y, t)|. \tag{3.6}$$

These imposed and induced groups are related through

$$Re_{slit}\, St_{slit} = Re\, St = 2\, Sh^2, \tag{3.7}$$

so the slit dynamics occupies the 2-D (St_{slit}, Re_{slit}) plane, on which lines of constant Sh are hyperbolae.

Figure 7 illustrates how the imposed parameter space maps onto the induced in-slit parameter space at $ISPL = 150$ and 120 dB. The imposed parameter space in figure 7(*a*) forms a rectangular grid, comprising three rows of constant *Re* (constant μ) and seven columns of constant forcing frequency. This grid becomes distorted in the induced plane, and lines of constant *Sh* provide an undistorted reference, as shown in figures 7(*b*) and 7(*c*). Further details on the in-slit velocity scales are provided in Appendix A. For $f \lesssim 4$ kHz, the in-slit Strouhal number remains nearly independent of *Re*, indicating that the induced velocity response scales approximately with the forcing frequency over this range. The in-slit Reynolds number largely retains its scaling with the imposed *Re* while decreasing overall as the acoustic frequency increases. These trends show that the induced Strouhal and Reynolds numbers are ordered by the imposed Strouhal and Reynolds numbers. Because the local slit dynamics is governed by the induced in-slit parameters, we report trends in both the induced and the imposed variables; the imposed parameters additionally serve as labels for the overall trends, as they are the directly prescribed operating conditions.

This mapping is a calibrated response relation for the present slit geometry and porosity, not a universal predictor. In particular, as $u_{slit}(f, \mu, ISPL)$ is geometry specific and the acoustic impedance depends on ISPL, the induced in-slit conditions must be determined from the realised flow response for each prescribed operating condition.

The acoustic frequencies considered here span a broad range of vortex-formation regimes (Ingard & Labate 1950; Aulitto 2023). At $ISPL = 150$ dB, the lowest frequency, $f = 500$ Hz, gives $St_{slit} \approx 0.04$, so that the slit width is much smaller than the oscillatory displacement. This corresponds to a strongly nonlinear regime, in which vortices are shed from the slit and convect away. At the highest frequency considered, $St_{slit} = O(1)$, and the vortices that form remain localised near the slit openings. At $ISPL = 120$ dB, St_{slit} ranges from $O(1)$ to approximately 50, consistent with the observed suppression of vortex formation. Over the same band, the shear number spans $Sh \approx 5$–28, so the Stokes layer remains thin relative to the slit ($Sh \gg 1$) and a distinct edge shear layer is present throughout, in contrast to the viscous-dominated micro-slit regime ($Sh \approx 1$–4) of Aulitto *et al.* (2022).

3.4. *Acoustic absorption*

Following the method outlined in § 2.3, we compute and present the power absorption coefficient in figure 8 to compare the total energy absorption at varying parameter combinations. At $ISPL = 150$ dB, for larger Re, the α is larger. Power absorption at $Re = Re_0$ is approximately 0.01 and 0.02 larger than at $Re = Re_0/2$ and $Re = Re_0/3$, respectively. On the contrary, for larger Re (i.e. lower viscosity), α is smaller at $ISPL = 120$ dB. Power absorption at $Re = Re_0$ is approximately 0.015 and 0.03 smaller than at $Re = Re_0/2$ and $Re = Re_0/3$, respectively.

The dependence of α on both Re and Re_{slit} remains significantly weaker, by at least an order of magnitude, than its dependence on St at $ISPL = 150$ dB, where the variation of α across the frequency sweep exceeds 0.4. On the contrary, at $ISPL = 120$ dB, the Re-dependence becomes comparable to the St-dependence, reflecting that, in the absence of strong vortex shedding, the absorption is dominated by the VL, and not by the frequency-dependent dynamics. In sum, figure 8 shows two distinct absorption regimes: a vortex-dominated regime at high ISPL, where St is the primary dominating parameter, and a viscosity-dominated regime at low ISPL, where Re plays a comparable role.

To complement the absorption spectra and to provide designers with information on the partition between reflected and transmitted acoustic power, we report the power reflection $|\widehat{R}|^2$ and transmission coefficients $|\widehat{T}|^2$ in figure 9. Across all cases, $|\widehat{R}|^2$ increases monotonically with St, while $|\widehat{T}|^2$ decreases. At low $St/St_0 \approx 1$, the $ISPL = 120$ dB cases are predominantly transmitting the power ($|\widehat{T}|^2 \approx 0.8$) with weak reflection ($|\widehat{R}|^2 \approx 0.1$), whereas at $ISPL = 150$ dB transmission is substantially reduced. At $St/St_0 > 8$, the slit is predominantly reflecting comparable power for both ISPLs, with $|\widehat{R}|^2 > 0.8$ and $|\widehat{T}|^2 < 0.1$. The ISPL dependence is weaker, especially for the transmitted power, at higher forcing frequencies ($St/St_0 > 8$). Variations with Re are comparatively modest over the range considered, indicating that St and ISPL primarily set the partition between reflected and transmitted power in this configuration.

The present DNS serves as a design tool for a slit–cavity configuration. We compare the slit impedance under different imposed operating conditions, even under the constraint of the anechoic termination.

Following Aulitto *et al.* (2022), we characterise the slit transfer impedance based on the complex acoustic pressure drop across the slit measured by the three probes divided by the volume flux through it, referenced to the in-slit velocity through the porosity

$$\widehat{Z}_{slit} = \frac{\widehat{p}_{left} - \widehat{p}_{right}}{\rho c\, \widehat{u}_{slit}} = \sigma\, (\widehat{Z}_s - \widehat{Z}_{ter}), \tag{3.8}$$

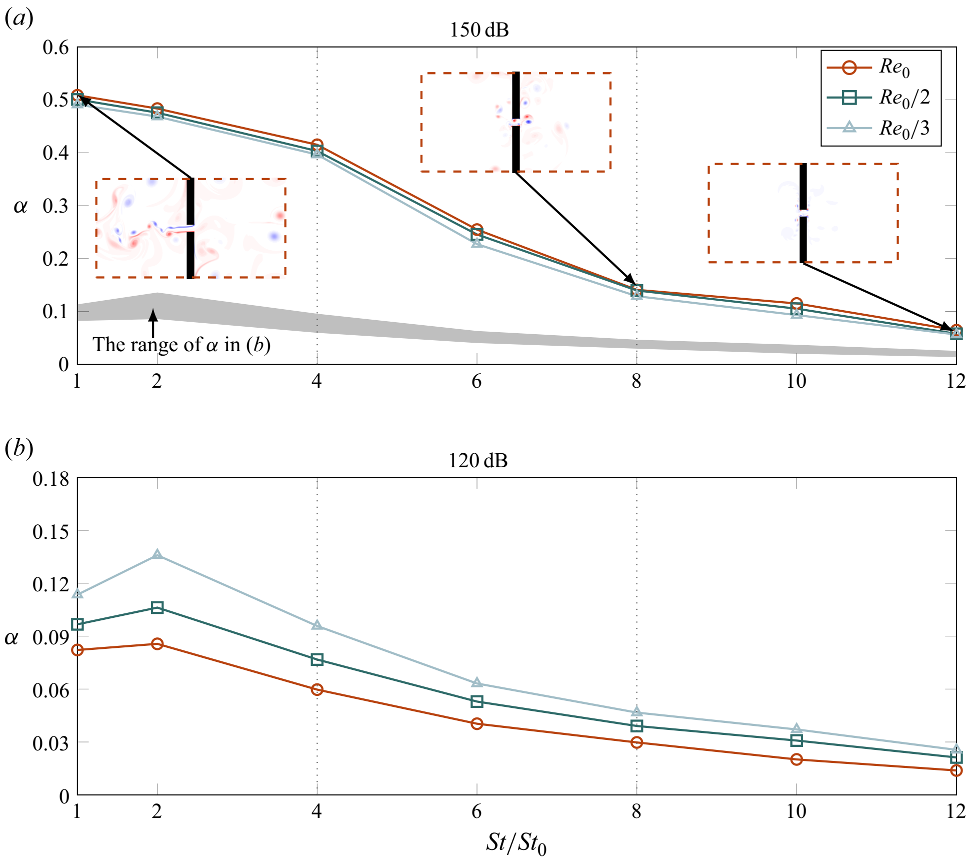

Figure 8. The power absorption coefficients $\alpha \equiv 1 - |\widehat{R}|^2 - |\widehat{T}|^2$ across all the *St*–*Re* combinations listed in table 1, subject to (*a*) $ISPL = 150$ dB and (*b*) $ISPL = 120$ dB. Probe locations are given in figure 2. The shaded zone in (*a*) demonstrates the range of α at $ISPL = 120$ dB, which is plotted in (*b*). Insets in (*a*) show the normalised instantaneous vorticity fields, $\boldsymbol{\omega}(\mathsf{x}; t_i)$, of cases (*a*, *i*), (*a*, *iii*) and (*a*, *iv*) in figure 30 to highlight the change in vorticity field across the range of α observed as *St* increases for $ISPL = 150$ dB and $Re = Re_0$.

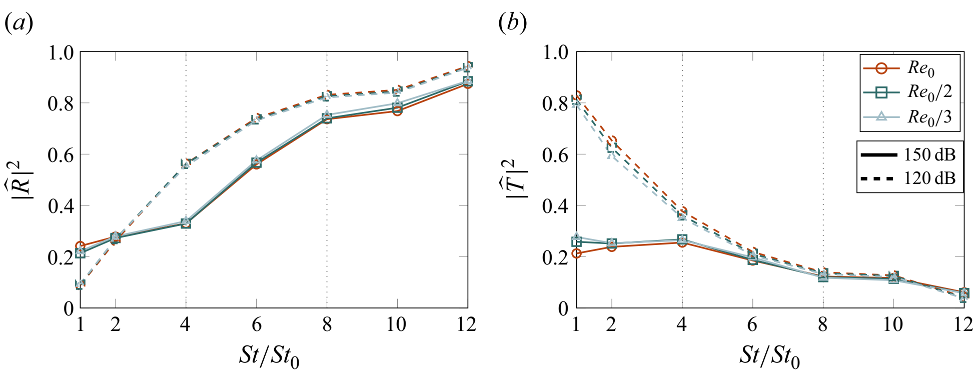

Figure 9. Incident acoustic energy-loss characteristics across the *St*–*Re*–*ISPL* combinations listed in table 1: (*a*) power reflection, $|\widehat{R}|^2$; and (*b*) power transmission coefficients, $|\widehat{T}|^2$.

https://doi.org/10.1017/jfm.2026.11896 Published online by Cambridge University Press

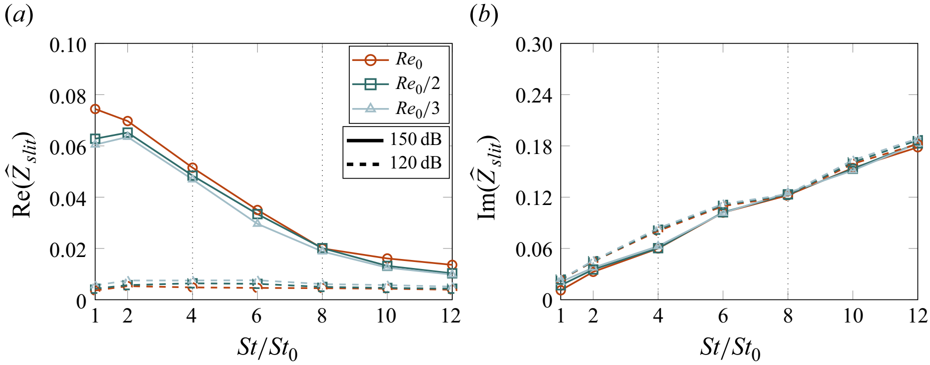

Figure 10. Slit transfer impedance, $\widehat{Z}_{slit}$, across the cases of table 1: (*a*) resistance Re($\widehat{Z}_{slit}$), evaluated from (3.10), and (*b*) reactance Im($\widehat{Z}_{slit}$), from (3.9).

with the porosity $\sigma = o/H$, the sample-loaded surface impedance, $\widehat{Z}_s = (1+\widehat{R})/(1-\widehat{R})$, obtained from the reflection coefficient (Chung & Blaser 1980) and the downstream termination impedance, $\widehat{Z}_{ter}$. As the computational domain is terminated anechoically, $\widehat{Z}_{ter} = 1$ and

$$\widehat{Z}_{slit} = \sigma\left(\frac{1+\widehat{R}}{1-\widehat{R}} - 1\right), \tag{3.9}$$

which references the impedance to the slit, rather than the slit surface, and removes the radiation load of the downstream anechoic termination. This is the empirical slit transfer impedance of Aulitto *et al.* (2022), here evaluated at the driving frequency in the compressible finite-amplitude regime.

The resistance is a small quantity relative to the reactance, so evaluating it from the difference $\mathrm{Re}(\widehat{Z}_s) - 1$ is poorly conditioned at high shear number. Following Aulitto *et al.* (2022), we instead define the resistance through the time-averaged dissipated power, $\langle P_{slit}\rangle = (1/2)\,\mathrm{Re}(\widehat{Z}_{slit})\,\rho c\,|\widehat{u}_{slit,\,pk}|^2$. Equating this to the absorption coefficient $\alpha = 1 - |\widehat{R}|^2 - |\widehat{T}|^2$ gives

$$\mathrm{Re}(\widehat{Z}_{slit}) = \sigma\,\frac{\alpha}{|1-\widehat{R}|^2} = \sigma\,\frac{1-|\widehat{R}|^2-|\widehat{T}|^2}{|1-\widehat{R}|^2}, \tag{3.10}$$

which is independent of the downstream reference plane.

Figure 10 reports Re($\widehat{Z}_{slit}$) and Im($\widehat{Z}_{slit}$) versus the peak in-slit velocity $u_{slit,pk}$ for both excitation levels and the three Reynolds numbers. The resistance increases by roughly an order of magnitude as $u_{slit,pk}$ grows between $ISPL = 120$ and 150 dB, consistent with the nonlinear-resistance growth of Ingard & Labate (1950) and with the amplitude dependence measured by Aulitto *et al.* (2022).

Figure 11 shows the slit resistance against the peak velocity, $u_{slit,pk}$, and slit Strouhal number, $St_{slit} = 2\pi f_s o/u_{slit,\,pk}$. At 150 dB, figure 11(*a*) indicates the peak velocity is larger for higher *Re*, which leads to slightly larger resistance. As St_{slit} decreases while the in-slit velocity grows, figure 11(*b*) shows the resistance rises by roughly a factor of four over the range sampled. At 120 dB, figure 11(*c*) indicates the peak velocity is nearly independent of *Re* and the resistance, dominated by viscous attenuation, is larger at lower *Re*. Figure 11(*d*) shows the resistance varies weakly with St_{slit}. The resistance rises by roughly an order of magnitude between $ISPL = 120$ and 150 dB, consistent with the nonlinear-resistance growth reported by Ingard & Labate (1950).

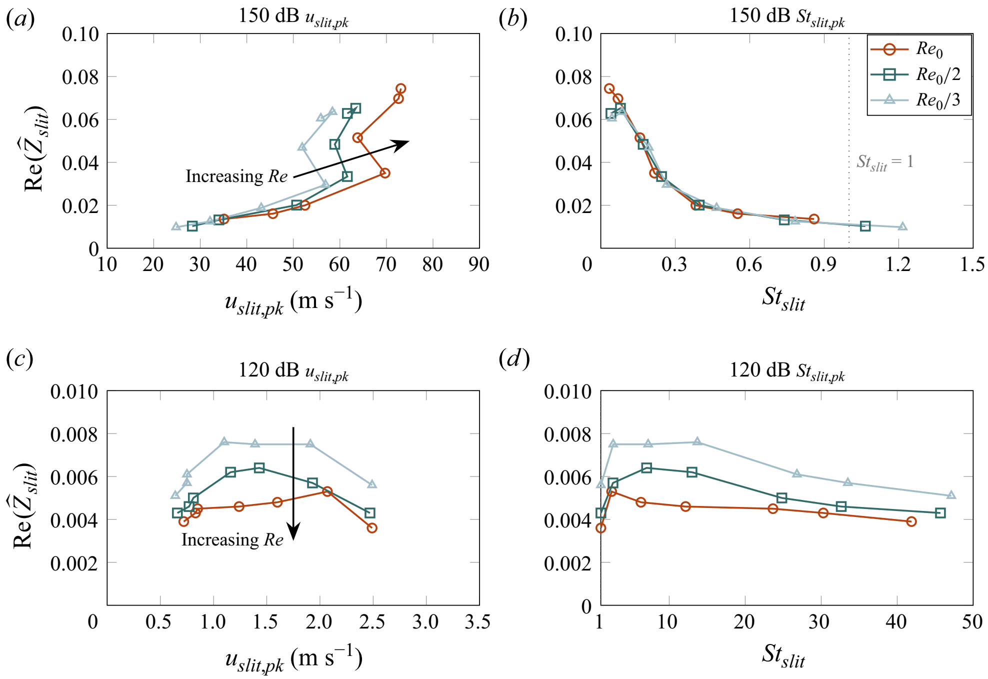

Figure 11. Slit resistance $\mathrm{Re}(\widehat{Z}_{slit})$ as a function of (*a*) the slit peak velocity $u_{slit,pk}$ and (*b*) slit Strouhal number St_{slit} at $ISPL = 150$ dB, and (*c*) the slit peak velocity $u_{slit,pk}$ and (*d*) slit Strouhal number St_{slit} at $ISPL = 120$ dB.

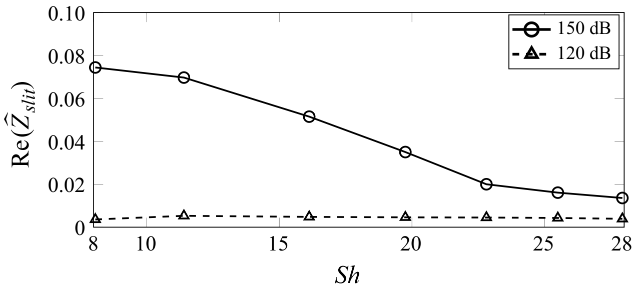

Figure 12. Slit resistance $\mathrm{Re}(\widehat{Z}_{slit})$ as a function of the shear number Sh at $Re = Re_0$. The resistance increases by roughly an order of magnitude from $ISPL = 120$ dB to $= 150$ dB at $Sh < 20$, recovering the nonlinear-resistance behaviour of Ingard & Labate (1950) and the ISPL dependence measured by Aulitto *et al.* (2022).

Figure 12 shows the slit resistance versus shear number at $Re = Re_0$. At 150 dB the resistance is smaller with larger Sh, whereas at 120 dB it is nearly independent of Sh. This contrast between a strongly amplitude- and frequency-dependent resistance at high ISPL and a weakly varying resistance at low ISPL is qualitatively consistent with the impedance-tube measurements of Aulitto *et al.* (2022) at a shear number range of 1–4 and ISPL range of 83–118 dB for micro-slit absorbers.

These resistance trends are a direct expression of the vortex-formation regime that the operating conditions occupy, which the in-slit Strouhal number and shear number make explicit. The two ISPLs occupy complementary parts of this range. At 150 dB, St_{slit} rises

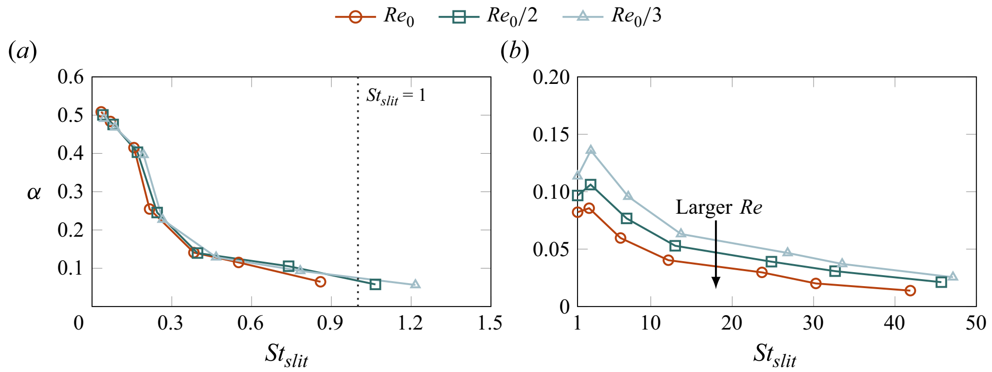

Figure 13. Power absorption coefficient $\alpha \equiv 1 - |\widehat{R}|^2 - |\widehat{T}|^2$ versus the in-slit Strouhal number St_{slit} for the three Reynolds numbers at (*a*) *ISPL* = 150 dB and (*b*) 120 dB. At high amplitude the three curves collapse onto a single function of St_{slit}; at low amplitude they retain a *Re* dependence characteristic of the viscous regime.

from ≈ 0.04 at 500 Hz to ≈ 1 at 6 kHz. According to Ingard & Labate (1950), the slit moves from strongly nonlinear vortex shedding toward the onset of vortices, which has been demonstrated in figure 5. At 120 dB, St_{slit} starts near unity and grows to ≈ 50, carrying the slit from the moderate vortex regime into the linear regime in which the resistance is nearly independent of *Sh*. Therefore, the band f_s =0.5–6 kHz covers the full sequence of vortex-formation regimes, from strongly nonlinear shedding through the moderate regime to the linear regime dominated by viscous attenuation.

Figure 13 recasts the power absorption coefficient against the in-slit Strouhal number. At 150 dB, the three Reynolds numbers collapse onto a single curve, so the high-amplitude absorption is set by St_{slit}: it is largest for $St_{slit} \lesssim 0.1$, where vortex shedding is strongest, and falls toward $St_{slit} = 1$. At 120 dB, the curves do not collapse and retain a clear *Re* dependence, so in the viscous regime the shear number, not St_{slit}, sets the loss.

For an acoustically compact slit ($2\pi f d/c \ll 1$), it can be considered as an elemental input within a lumped-impedance framework (e.g. in perforated plates by Melling (1973) and Aulitto (2023)) to estimate the response of a complex configuration. Given the constraint that slit resistance depends on the local velocity at the slit mouth, which in a resonator differs from the incident particle velocity, the present work can also support a self-consistent evaluation when the ISPL conditions bracket a range of in-slit amplitudes that a cavity-backed configuration may realise.

The analysis domain is confined to $\Omega = [x/d, y/d] \in [-14, 14] \times [-14, 14]$ for $St/St_0 \leq 8$ and $\Omega = [x/d, y/d] \in [-11.2, 11.2] \times [-14, 14]$ for $St/St_0 \geq 10$. The horizontal distribution of VL identifies the region containing more than 99 % of the total VL. Within this region, more than 99 % of the total KE associated with the induced flow field is retained, giving the spatial extent used henceforth for spectral analysis.

This database is directly relevant to real-world engineering design scenarios involving sound at different ISPLs and frequencies in different media with different viscosities. The ISPL sets the magnitude of the imposed velocity oscillation through the plane wave approximation of acoustic impedance $u \approx p/\widehat{z}$, where $\widehat{z} = \rho c$ is the characteristic acoustic impedance of air. The velocity magnitude scales the vorticity field Mach number, and thus the importance of compressible effects and nonlinear interactions. The acoustic frequency is introduced through the Strouhal number, which compares the convective time scale of the vorticity field with the flow oscillation period. A combination of both parameters determines the presence of sound sources with varying amplitudes and frequencies. The

https://doi.org/10.1017/jfm.2026.11896 Published online by Cambridge University Press

wavelength of the Stokes layer λ_s depends on the Reynolds number with a similarity $\lambda_s \sim d/\sqrt{Re\, St}$. Different slit thickness will change Re and St as well. To separate the effects attributed to Re and St, we vary the fluid property dynamic viscosity to adjust for varying Re.

4. Spectral analysis of the DNS data

Previous methods typically quantify overall dissipation in an integral sense, similar to power absorption coefficients (Tam *et al.* 2001), and thus often overlook both the spatial and spectral structure of acoustic energy dissipation and its associated energy budget. To address this, we use SPOD to decompose the acoustic-induced flow-field fluctuations into optimally energy-ranked coherent spectral flow structures. This analysis enables separate, mode-by-mode investigation of the KE and VL contributions at each frequency, together with their corresponding coherent spatial structures. Spatial or spectral integration is then used to recover the overall integral behaviour, enabling a better understanding of the acoustic energy dissipation mechanism.

4.1. *Spectral proper orthogonal decomposition*

Consider a time series consisting of N_t snapshots. Each snapshot is represented by an observable state vector $\mathsf{y} \in \mathbb{C}^N$, where N is the dimension of the data. In line with common practice in the analysis of compressible turbulence (Kida & Orszag 1990; Wang *et al.* 2013), the observable is the fluctuating density-weighted velocity field, defined as

$$\mathsf{y}(\mathsf{x};\, t) = \sqrt{\beta(\mathsf{x};\, t)}\, \mathsf{u}(\mathsf{x};\, t), \tag{4.1}$$

where $\beta = \rho/\rho_0$ is the dimensionless density ratio at each spatial location (a scalar), and β denotes its spatially discretised array representation, quantifying deviations from the nominal reference density, ρ_0. With this definition, the total KE within the computational domain can be expressed using the energy norm $\|\cdot\|_y$, induced by the inner product, as

$$K \equiv \int_\Omega \frac{1}{2}\beta(\boldsymbol{x})\boldsymbol{u}^H(\boldsymbol{x})\boldsymbol{u}(\boldsymbol{x})\, \mathrm{d}\boldsymbol{x} \approx \frac{1}{2}\mathsf{y}^H \boldsymbol{W}_y \mathsf{y} = \frac{1}{2}\langle \mathsf{y}, \mathsf{y}\rangle_y \equiv \frac{1}{2}\|\mathsf{y}\|_y^2. \tag{4.2}$$

Here, $\boldsymbol{W}_y$ is a Hermitian positive–definite weight matrix for the discrete approximation of the volume integral, $\sum_\Omega(\cdot)\Delta_x\Delta_y$, and $(\cdot)^H$ denotes the Hermitian transpose. The density ratio is introduced solely as a weighting function for the velocity field. For nearly incompressible flows, as in the present configuration, density variations are weak, and their weighting has only a minor effect ($\beta \approx 1$). Nevertheless, we retain this formulation to account for the contributions of both velocity and density fluctuations to the dissipation.

We seek spatio-temporal structures that optimally represent the spectral content of y, expressed through its Fourier expansion

$$\mathsf{y}(t) = \sum_{n=-\infty}^{\infty} \widehat{\mathsf{y}}_n \mathrm{e}^{i2\pi f_n t}. \tag{4.3}$$

Assuming ergodicity in statistically stationary flows, we apply Welch's method (Welch 1967) to obtain convergent estimates of the spectral densities. Specifically, the time series is divided into N_{blk} blocks, each containing N_{DFT} consecutive snapshots separated by a constant time step Δt. Adjacent blocks may overlap by N_{ovlp} snapshots. Guidance on the appropriate selection of these parameters is provided in Schmidt & Colonius (2020). In practice, the mth block, for $m = 1, 2, \ldots, N_{blk}$, is constructed as

$$\mathsf{y}^{(m)} = \begin{bmatrix} \mathsf{y}_1^{(m)} & \mathsf{y}_2^{(m)} & \cdots & \mathsf{y}_{N_f}^{(m)} \end{bmatrix} \in \mathbb{C}^{N \times N_{DFT}}, \tag{4.4}$$

and its discrete Fourier transform (DFT) along the temporal domain is denoted by

$$\widehat{\boldsymbol{Y}}^{(m)} = \begin{bmatrix} \widehat{\mathsf{y}}_1^{(m)} & \widehat{\mathsf{y}}_2^{(m)} & \cdots & \widehat{\mathsf{y}}_{N_f}^{(m)} \end{bmatrix}. \tag{4.5}$$

Here, only the non-negative Fourier components are collected due to the reality of the data, yielding $N_f = \lfloor N_{DFT}/2 \rfloor + 1$ frequency components. For each frequency index $n = 1, 2, \ldots, N_f$, the ensemble of N_{blk} Fourier realisations at frequency f_n across all data blocks forms a data matrix

$$\widehat{\boldsymbol{Y}}_n = \begin{bmatrix} \widehat{\mathsf{y}}_n^{(1)} & \widehat{\mathsf{y}}_n^{(2)} & \cdots & \widehat{\mathsf{y}}_n^{(N_{blk})} \end{bmatrix}. \tag{4.6}$$

The corresponding cross-spectral density matrix is

$$\boldsymbol{S}_n \equiv \frac{1}{N_{blk}} \widehat{\boldsymbol{Y}}_n \widehat{\boldsymbol{Y}}_n^H. \tag{4.7}$$

The eigenvectors, $\widehat{\boldsymbol{\Xi}}_n$, and the eigenvalues, $\boldsymbol{\Lambda}_n$, of the eigenvalue problem

$$\boldsymbol{S}_n \boldsymbol{W}_y \widehat{\boldsymbol{\Xi}}_n = \boldsymbol{\Lambda}_n \widehat{\boldsymbol{\Xi}}_n, \tag{4.8}$$

give the SPOD modes and their corresponding modal energy. The SPOD modes are the columns of $\widehat{\boldsymbol{\Xi}}_n$, denoted by $\widehat{\boldsymbol{\xi}}_n^{(k)}$, where k is the column index. The eigenvalues are sorted in decreasing order of energy (by singular value) as

$$\lambda_n^{(1)} \geq \lambda_n^{(2)} \geq \cdots \geq \lambda_n^{(N_{blk})}. \tag{4.9}$$

At the same frequency, the SPOD modes are mutually orthogonal as

$$\langle \widehat{\boldsymbol{\xi}}_n^{(k_1)}, \widehat{\boldsymbol{\xi}}_n^{(k_2)} \rangle_y = \delta_{k_1,k_2}, \tag{4.10}$$

and are optimal for modal energy under the norm induced by (4.2). Here, $\delta_{\cdot,\cdot}$ is the Kronecker delta function, and the indices $k_1, k_2 = 1, 2, \cdots, N_{blk}$ refer to the modal ranks. We refer the reader to Towne *et al.* (2018) for more details of SPOD. Spectral proper orthogonal decomposition provides an optimal decomposition of each realisation of the flow field into energy-ranked structures as

$$\widehat{\mathsf{y}}_n = \sum_{k=1}^{N_{blk}} a_n^{(k)} \widehat{\boldsymbol{\xi}}_n^{(k)}, \quad \text{where} \quad a_n^{(k)} \equiv \langle \widehat{\boldsymbol{\xi}}_n^{(k)}, \widehat{\mathsf{y}}_n \rangle_y, \tag{4.11}$$

is the corresponding SPOD expansion coefficient. Across different ranks at a given frequency, the SPOD expansion coefficients are uncorrelated (Nekkanti & Schmidt 2021*b*; Chu & Schmidt 2025), that is

$$\mathrm{E}\left\{ \left(a_n^{(k_1)}\right)^H a_n^{(k_2)} \right\} = \lambda_n^{(k_1)} \delta_{k_1,k_2}. \tag{4.12}$$

4.2. *Representative SPOD eigenvalue spectrum and modes*

Spectral analysis is performed on the reduced domain $\varOmega$ defined and justified in § 3.2. The SPOD sampling interval, Δt_{spod}, is set to 2000 simulation time steps for $St \leq 8St_0$ and 1500 time steps for $St \geq 10St_0$. The SPOD is performed using 640 snapshots ($N_t = 640$), partitioned into nine blocks with 87.5 % overlap with a block length $N_{DFT} = 320$.

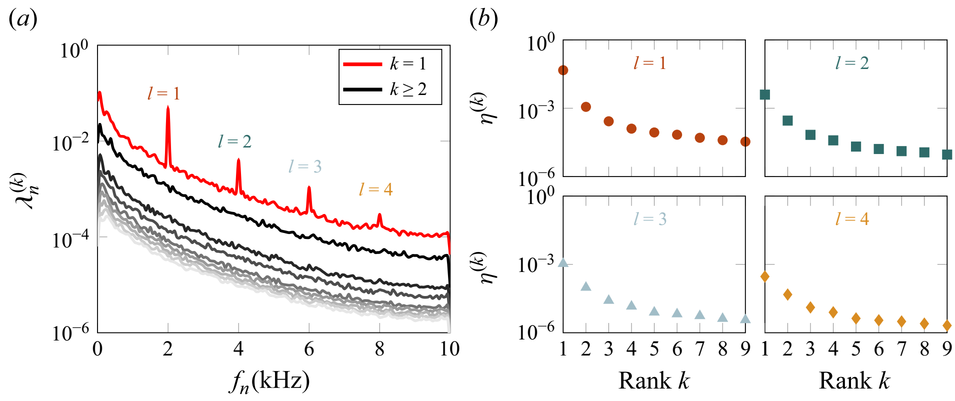

Figure 14. The SPOD-based spectral energy analysis for $ISPL = 150$ dB, $St = 4St_0$ and $Re = Re_0$: (*a*) eigenvalue spectra, $\lambda_n^{(k)}$; and (*b*) energy associated with each rank, $\eta^{(k)}$, at four harmonic frequencies ($l = 1$–4 defined in (4.13)).

A rectangular window is used because the acoustic signal is periodic within each analysis segment. Spectral convergence is confirmed by the large separation between the leading and suboptimal SPOD eigenvalues, indicating accurate identification of dominant coherent structures.

As an example, figure 14(*a*) shows the SPOD eigenvalue spectrum for the case of 150 dB with a Reynolds number of Re_0, where the imposed acoustic frequency $f_s = 2$ kHz corresponds to a Strouhal number of $St = 4St_0$. The SPOD eigenvalues of the leading rank exhibit four tonal peaks of decreasing magnitude at integer multiples of f_s, implying a harmonic response. We introduce the harmonic index

$$l \equiv f_n/f_s, \tag{4.13}$$

such that the fundamental frequency corresponds to $l = 1$ and higher-order harmonics are given by $l = 2, 3, \cdots, \lfloor (1/(2\Delta t_{spod} f_s)) \rfloor$, up to the Nyquist limit. These spectral peaks indicate the presence of coherent vortex shedding triggered by the imposed acoustic excitation (Tam *et al.* 2001, 2005). The remaining eigenvalues form a broadband spectrum that decreases monotonically. This behaviour is characteristic of mixed broadband–tonal flows, whose complex dynamics combines both stochastic and deterministic features.

Figure 14(*b*) shows the distribution of energy across the mode ranks for the four tonal peaks. The magnitude of the leading SPOD rank is at least one order of magnitude larger than that of the suboptimal ranks. This pronounced separation reflects the distinct low-rank dynamics of the flow field. As later shown in figure 16, these trends are qualitatively consistent across all parameter combinations listed in table 1. We define the contribution of each rank k, for $k = 1, 2, \cdots, N_{blk}$, via the energy fraction as

$$\eta^{(k)} = \sum_n \eta_n^{(k)} = \frac{\sum_n \lambda_n^{(k)}}{\sum_n \sum_k \lambda_n^{(k)}}, \tag{4.14}$$

which measures the portion of modal energy. Accordingly, we focus on the first three ranks, which represent 95 %, 3.5 % and 1 % of the total energy, respectively. Collectively, these three modes account for 99 % of the energy across the examined parameter combinations. Contributions from higher-order suboptimal modes are neglected in the spectral analysis because of their low energy content.

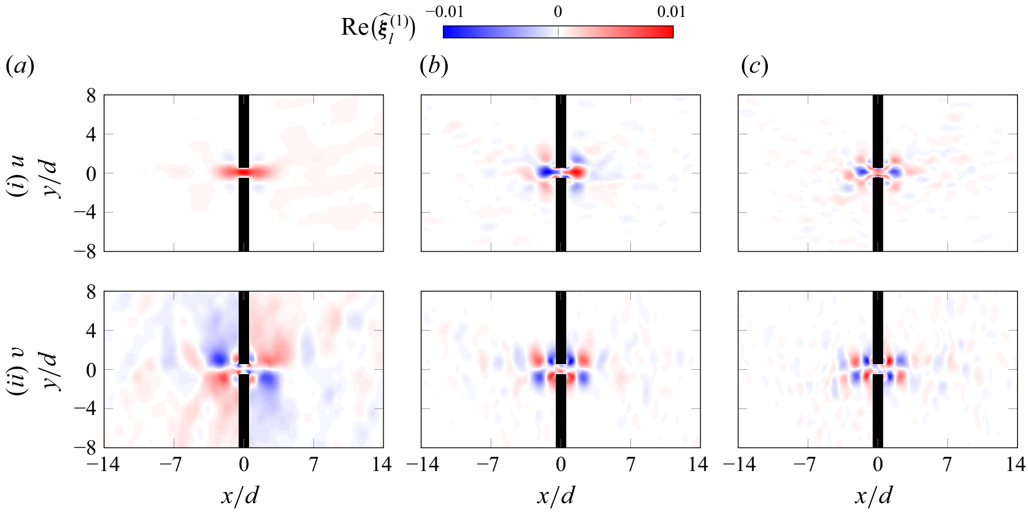

Figure 15. Leading SPOD modes, Re($\hat{\boldsymbol{\xi}}_l^{(1)}$), at $ISPL = 150$ dB, $St = 4St_0$ and $Re = Re_0$. Cases in (*a*)–(*c*) correspond to $l = 1$, 2 and 3. Cases in (*i*) and (*ii*) correspond to velocities in the x- and y-coordinate directions, u and v.

Figure 15 shows the leading fundamental, 2nd and 3rd harmonic SPOD modes for the case examined in figure 14. The spatial structures are active both upstream and downstream of the slit, reflecting the periodic nature of the acoustically driven flow field. Across all harmonics, the modes are concentrated near the slit, with pronounced intensities at the four slit corners. These localised structures highlight strong interactions between the flow and the slit geometry. In particular, the induced oscillatory boundary-layer dynamics enables the conversion of incident acoustic energy into coherent vortical motion. As expected, the spatial modes exhibit smaller-scale structures as the harmonic order increases. This trend is consistent with the higher effective excitation frequencies associated with harmonic tones, which induce faster oscillations in the flow field.

The slight asymmetry of the modes about the horizontal centreline, especially in the y-direction velocity component, is consistent with observations from previous analyses based on both numerical simulations (Qiang *et al.* 2022) and experimental measurements (Tang *et al.* 2025). Since the configuration is geometrically symmetric about the centreline, it reflects the dominant coherent structures captured by SPOD rather than a strict symmetry breaking of the statistically averaged flow. In the instantaneous vorticity field in figure 5(*a*), vortex shedding is not symmetric with respect to the centreline, and the leading SPOD modes inherit this pattern. Such asymmetric coherent structures may subsequently be amplified through nonlinear vortex interactions (Mizushima & Hatsuda 2014; Frantz *et al.* 2025). Nevertheless, full statistical convergence is more difficult to achieve in regimes with stronger broadband content (lower St and higher Re), and additional data would further sharpen the modes in that range.

4.3. *Spectral features across the parameter space*

To understand the spectral behaviour, we compare the SPOD eigenvalue spectra across the parameter space at $ISPL = 150$ dB, as shown in figure 16. In general, the harmonic peaks become more distinct from the broadband content for smaller Re. This trend is consistent with the reduced spectral density at lower Re, which lowers the broadband energy level and thereby enhances the spectral contrast between coherent harmonic peaks

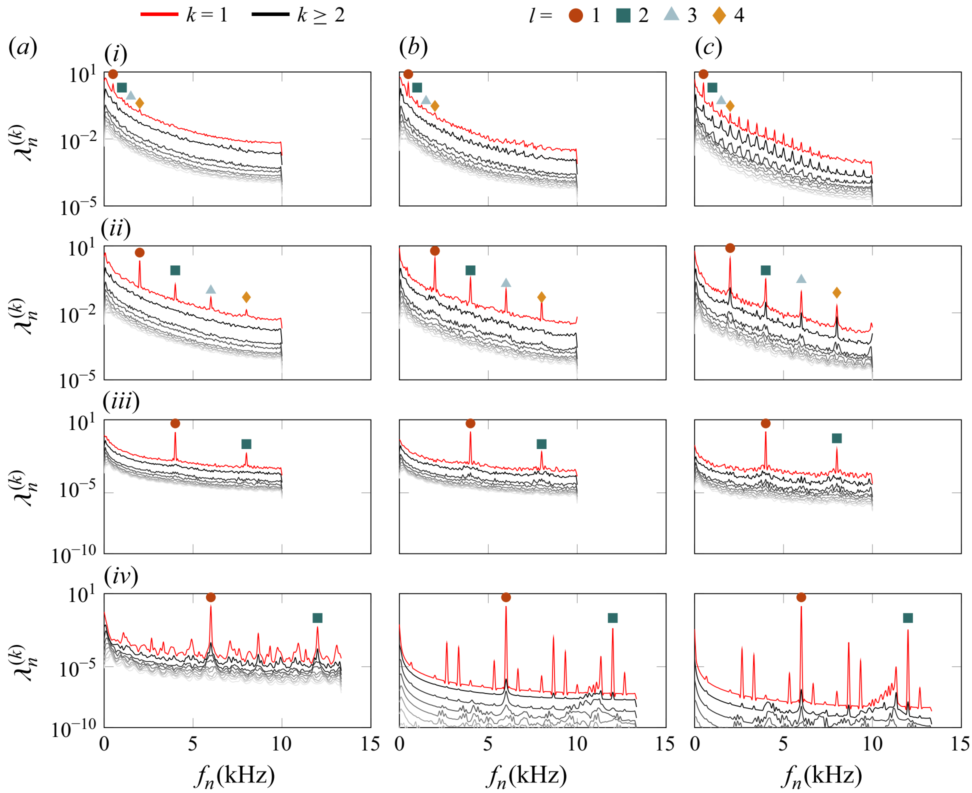

Figure 16. The SPOD eigenvalue spectra, $\lambda_n^{(k)}$, at different ranks k for different St–Re combinations at $ISPL =$ 150 dB. Cases in column (*a*)–(*c*) represent $Re = Re_0$, $Re_0/2$ and $Re_0/3$. Cases in row (*i*)–(*iv*) represent $St = St_0$, $4St_0$, $8St_0$and $12St_0$. The fundamental frequency ($l = 1$) and its higher-order harmonics ($l \geq 2$) manifest as peaks in the spectrum. For example, two tonal peaks arise at $f_n = 4$ kHz ($l = 1$) and $f_n = 8\,kHz$ ($l = 2$) in case (*a*, *iii*).

and incoherent broadband components. In addition, both the leading and suboptimal ranks exhibit more visible harmonic peaks at lower Re, without a reduction in the separation between their SPOD eigenvalues. This observation suggests that increased viscosity at smaller Re promotes the coherence of fluctuations at the forcing frequency across cycles, thereby suppressing broadband fluctuations.

An increase in acoustic excitation frequency also leads to stronger harmonic peaks. At $St = 12St_0$, additional peaks appear at non-integer multiples of the forcing frequency and become more pronounced at lower Re. These additional peaks suggest more complex nonlinear interactions within the flow field, involving not only vortex-shedding harmonics but also interactions with the slit boundaries. This behaviour can be qualitatively observed in the instantaneous fields shown in figure 5, where the shed vortices at $St = 12St_0$ travel along and interact with the y-direction boundaries of the slit, rather than propagating in phase with the acoustic wave.

Figure 17 presents the leading x-direction SPOD modes at their respective fundamental frequencies, corresponding to the cases shown in figure 16. The spatial axes follow the same convention as in figure 15, but are omitted here for clarity. At the lowest acoustic frequency of $St = St_0$, a decrease in Reynolds number leads to more flattened large-scale structures along the horizontal centreline, while the smaller-scale structures are

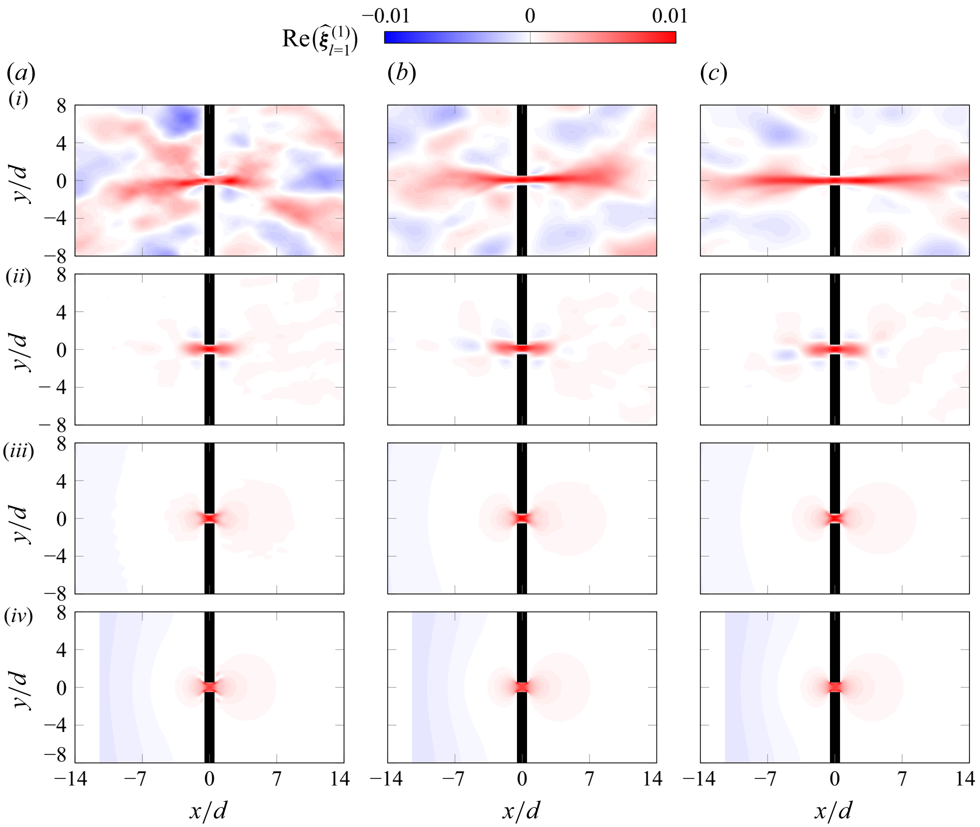

Figure 17. Leading SPOD modes, $\mathrm{Re}(\widehat{\boldsymbol{\xi}}^{(1)}_{l=1})$, for different St–Re combinations at $ISPL = 150\,\mathrm{dB}$, plotted at their respective fundamental frequencies ($l = 1$) as their x-directional components, u. Cases in column (*a*)–(*c*) represent $Re = Re_0$, $Re_0/2$ and $Re_0/3$. Cases in row (*i*)–(*iv*) represent $St = St_0$, $4St_0$, $8St_0$and $12St_0$.

diminished. Combined with the corresponding SPOD eigenvalue spectra, where lower-Re cases exhibit reduced broadband energy and more pronounced spectral peaks, these observations suggest that stronger viscous effects at this frequency enhance the coherence of vortex shedding. This enhancement occurs while suppressing the remaining flow content.

For larger acoustic frequency, the leading SPOD modes exhibit similarly compact spatial support near the slit, with reduced dependence on Re. Specifically, at $St = 4St_0$, the modes display dumbbell-shaped structures spanning the slit, whereas at $St = 8St_0$ and $12St_0$, they exhibit X-shaped patterns localised near the slit. With a virtually doubled slit thickness (i.e. the Womersly number Wo doubled), the case with $St = 8St_0$ and $Re = Re_0$ exhibits a more confined X-shaped pattern as opposed to the case with $St = 4St_0$ and $Re = Re_0/2$, which appears to be dumbbell shaped. Figure 31 in Appendix C documents the modal structures of the cases not shown in figure 17.

Taken together, these observations indicate that increasing the acoustic frequency or the slit thickness compresses the dominant vortex-shedding structures toward the near-slit region. At the same time, more confinement can introduce complex interactions near and within the slit.

To have a detailed understanding of mode structure inside the slit, we show the normalised velocity profiles at the inlet ($x = -d/2$), centre ($x = 0$) and outlet ($x = d/2$)

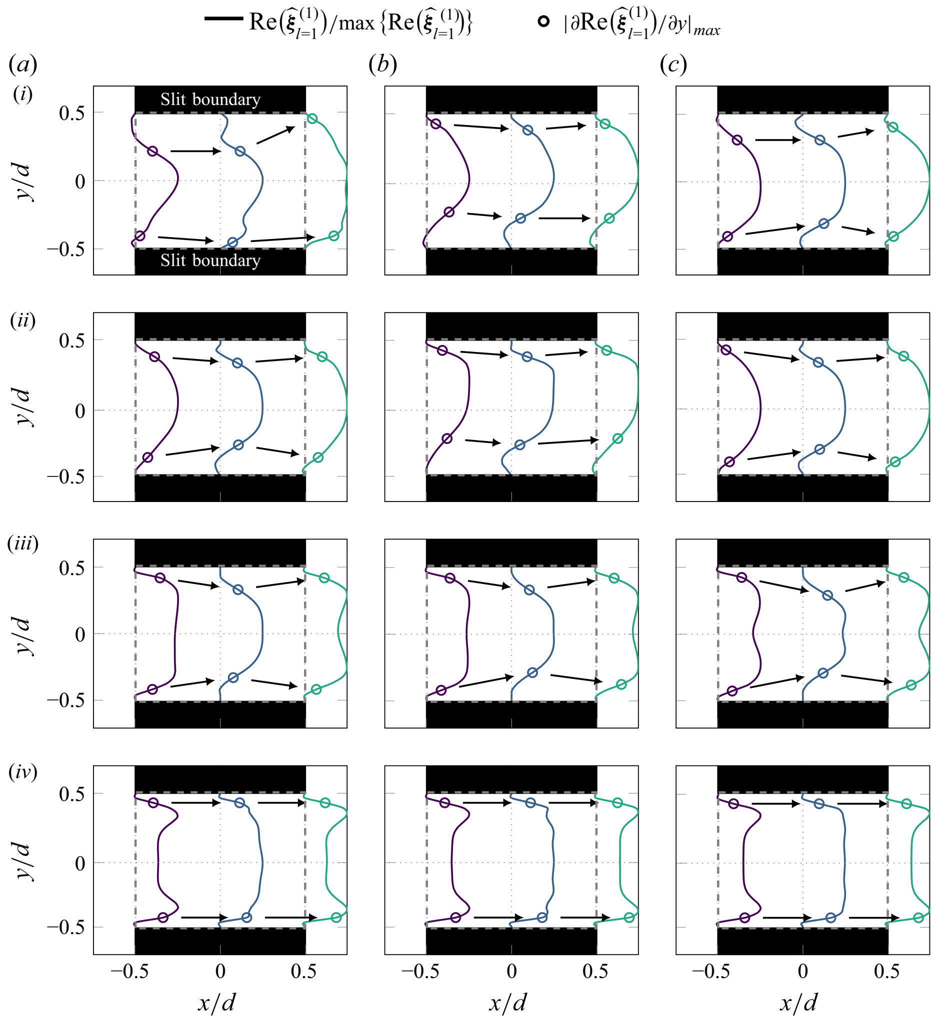

Figure 18. Profiles of the x-directional components, u, of the leading SPOD modes at the fundamental frequency, $\mathrm{Re}(\widehat{\boldsymbol{\xi}}^{(1)}_{l=1})/\max\{\mathrm{Re}(\widehat{\boldsymbol{\xi}}^{(1)}_{l=1})\}$, within the slit for different *St*–*Re* combinations at $ISPL = 150$ dB. The maximum mode gradient in the y direction on the top and bottom halves of each profile, $|\partial\mathrm{Re}(\widehat{\boldsymbol{\xi}}^{(1)}_{l=1})/\partial y|_{max}$, is marked as a hollow circle, which is connected by arrows across all the profiles. Cases in column (*a*)–(*c*) correspond to $Re = Re_0$, $Re_0/2$ and $Re_0/3$. Cases in row (*i*)–(*iv*) correspond to $St = St_0$, $4St_0$, $8St_0$ and $12St_0$.

of the slit in figure 18. For most *St*–*Re* combinations, the inlet and outlet profiles are nearly identical, indicating weak x-direction variation of the fundamental mode between the inlet and outlet. We calculated the mode gradient in the y direction using a first-order finite-difference approximation. We highlighted two points on each profile where the maximum mode gradients occur in both the top and bottom halves. These points have implications on the distribution of the VL field, which will be discussed in § 4.5. At the lower $St \leq 4St_0$ and higher $Re \geq Re_0/2$, the profiles are asymmetric about the horizontal centreline. In this regime, the oscillatory motion produces a thicker boundary layer, and we observe transient reversal of the wall shear stress and a localised flow detachment at the slit corner, consistent with the larger-scale mode structures seen in figure 17. In contrast, at $St > 4St_0$ and $Re < Re_0/2$, the profile is similar to the Womersley flow profile with a Womersley number $Wo \geq 16$ (Womersley 1955), exhibiting symmetrical structure according to the horizontal centreline. The increased acoustic frequency yields a thinner boundary layer.

4.4. *Three-dimensional effects*

The present database and SPOD-based energetics analysis are obtained from DNSs. This choice enables a broad sweep in ($ISPL$, St, Re) at tractable cost. Nevertheless, acoustic-driven slit flows may, in principle, develop a 3-D dynamics, including spanwise vortex stretching, secondary instabilities of shear layers and eventual breakdown to turbulence. Such mechanisms are excluded by construction in two dimensions and may alter both the near-slit vortex dynamics and the spatial distribution of dissipation under certain operating conditions. To assess the role of three-dimensionality, we compare the 2-D and 3-D simulations at $ISPL = 150$ dB, $Re = Re_0/3$ and $St = 2St_0$. Two 3-D slit configurations are examined, with spanwise extents $L_{z,1} = 11d$ and $L_{z,2} = 22d$, as described in figure 3.

We obtain $\alpha = 0.1628$ for the 2-D case and $\alpha = 0.1450$ for both 3-D cases, a difference of roughly 11 % that reflects the additional spanwise degrees of freedom in three dimensions. To enable direct comparison, an approximate spanwise average of the 3-D streamwise velocity field, $\langle u\rangle_z(x, y, t)$, is constructed by sampling 10 evenly spaced (x, y) planes across the span. The SPOD procedure described in § 4 is subsequently applied to $\langle u\rangle_z$, using $N_t = 320$ time snapshots instead of 640 in the main database, owing to the shorter 3-D simulation. As shown in figure 19(*a*), the leading SPOD mode of the 3-D simulation exhibits a near-slit spatial structure that is almost identical to that of the 2-D case, even for the shorter spanwise extent $L_{z,1} = 11d$. Figure 19(*b*) shows that, for this parameter combination, the leading SPOD eigenvalue spectrum from the 3-D cases is quantitatively consistent with the corresponding 2-D spectrum. Overall, these results suggest that the 2-D model for this configuration represents well the dominant flow structures and statistics.

A spanwise-wavenumber analysis further supports this interpretation. We quantify three-dimensionality by decomposing the x-component fluctuating velocity field into spanwise Fourier modes and quantifying the KE contained in each spanwise wavenumber. Figure 20 shows that the energy in non-zero spanwise wavenumbers remains negligible compared with the $k_z = 0$ component, indicating an effectively 2-D response for these cases. Together with the SPOD eigenvalue spectra and modes shown in figure 19, these results suggest that the 2-D DNSs can capture the dominant coherent structures and energetics observed in the corresponding 3-D simulations for the specific parameter combination examined, even at the high acoustic amplitude of $ISPL = 150$ dB. The subsequent flow analysis can therefore be effectively carried out in the two-dimensional domain at substantially reduced cost, without loss of the essential physics.

4.5. *Dissipation mechanism*

The two principal contributions to the energy budget associated with the consumption of the input acoustic energy are the KE, dominated by vortical dynamics at the shedding frequency, and the VL, spanning all frequency components (Tam & Kurbatskii 2000; Tam *et al.* 2001). Here, KE quantifies the energy stored in the flow over the analysis window, whereas VL quantifies the portion of energy irreversibly dissipated by viscosity. Accordingly, KE and VL are distinct quantities in the energy budget rather than overlapping dissipation channels: the KE of shed vortices will eventually be viscously dissipated, but this subsequent dissipation occurs outside the analysis window and is not double counted in VL. By decomposing the flow field into optimally energy-ranked SPOD modes, we analyse the respective KE and VL contributions of each spectral component.

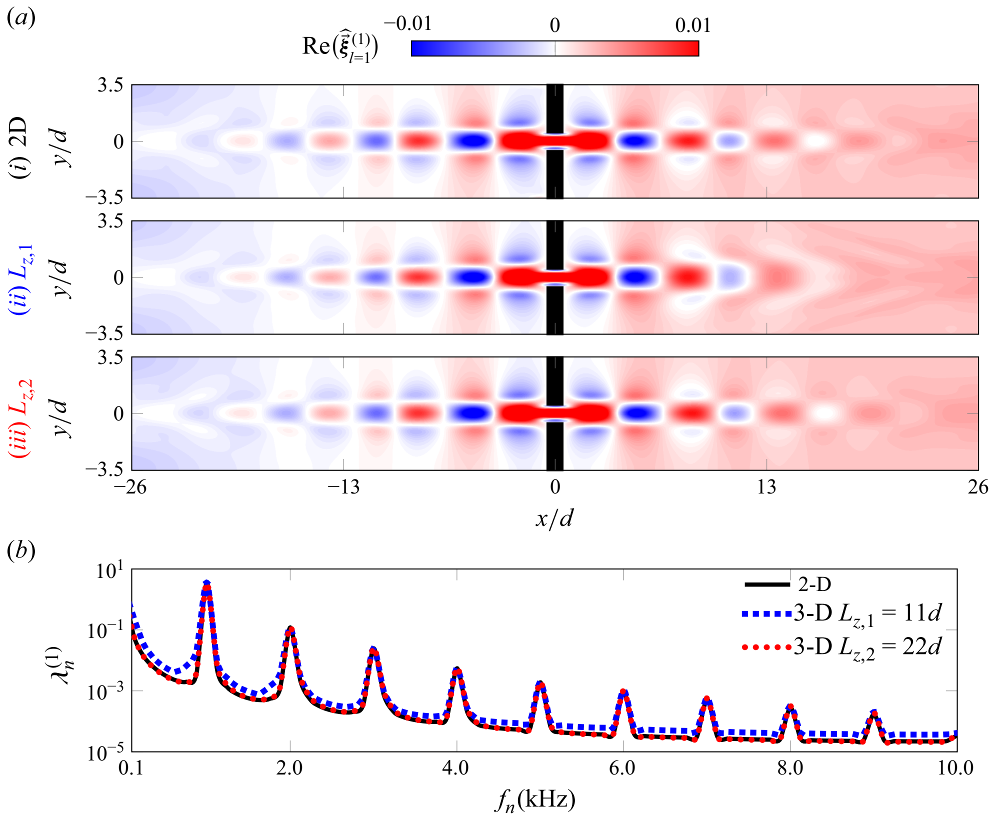

Figure 19. Comparison of the 2-D and 3-D simulation on (*a*) leading SPOD modes, $\mathrm{Re}(\widehat{\boldsymbol{\xi}}^{(1)}_{l=1})$ and (*b*) eigenvalue spectrum $\lambda_n^{(1)}$ at $ISPL = 150$ dB, $Re = Re_0/3$ and $St = 2St_0$ plotted at their respective fundamental frequencies ($l = 1$) as their x-directional components, u.

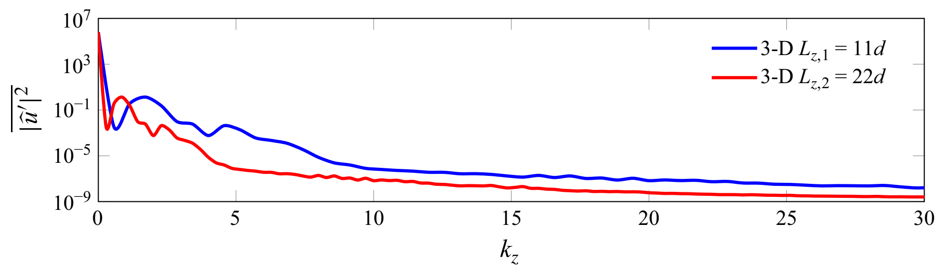

Figure 20. Spanwise Fourier decomposition of the fluctuating KE in the 3-D DNS. The energy is concentrated at the spanwise-uniform component ($k_z = 0$), with negligible contribution from non-zero spanwise wavenumbers, indicating an effectively 2-D response over the analysed interval.

For each frequency f_n, we express the velocity and stress tensor as linear combinations of the SPOD modes, $\widehat{\boldsymbol{\xi}}_n^{(k)}$, and corresponding expansion coefficients, a_n, as

$$\widehat{\mathsf{y}}_n(\mathsf{x}) \approx \sum_{k=1}^{3} a_n^{(k)} \widehat{\boldsymbol{\xi}}_n^{(k)}(\mathsf{x}), \quad \text{and} \quad \widehat{\mathsf{T}}_n(\mathsf{x}) \approx \sum_{k=1}^{3} a_n^{(k)} \widehat{\boldsymbol{T}}_n^{(k)}(\mathsf{x}), \tag{4.15}$$

https://doi.org/10.1017/jfm.2026.11896 Published online by Cambridge University Press

where

$$\widehat{\boldsymbol{T}}_n^{(k)}(\mathsf{x}) \equiv \frac{1}{\beta Re}\left[\nabla\widehat{\boldsymbol{\xi}}_n^{(k)} + \left(\nabla\widehat{\boldsymbol{\xi}}_n^{(k)}\right)^H - \frac{2}{3}\left(\nabla\cdot\widehat{\boldsymbol{\xi}}_n^{(k)}\right)\mathsf{I}\right](\mathsf{x}) \tag{4.16}$$

is the rank-k stress-tensor mode.

To enable a direct, dimensionally consistent comparison between the spectral KE and VL components, we weight the KE spectrum by the corresponding angular frequency, $\omega_n = 2\pi f_n$. This process converts the spectral KE density (energy per frequency) into an energy-rate scale (power per frequency) with units consistent with the spectral VL density. Frequency weighting is introduced to maintain dimensional consistency and facilitate comparison, whereas a budget interpretation requires applying the same scaling consistently to all terms of the spectral KE equation. The frequency-weighted spectral KE field can then be expressed as

$$\widehat{\boldsymbol{K}}_n(\mathsf{x}) = \frac{1}{2}\mathrm{E}\left\{\left[\omega_n\widehat{\mathsf{y}}_n^H\widehat{\mathsf{y}}_n\right](\mathsf{x})\right\} \approx \pi f_n \mathrm{E}\left\{\left[\left(\sum_{k=1}^{3} a_n^{(k)}\widehat{\boldsymbol{\xi}}_n^{(k)}\right)^H\left(\sum_{k=1}^{3} a_n^{(k)}\widehat{\boldsymbol{\xi}}_n^{(k)}\right)\right](\mathsf{x})\right\} \tag{4.17}$$

$$= \pi f_n \mathrm{E}\left\{\sum_{k_1=1}^{3}\sum_{k_2=1}^{3}\left[\left(a_n^{(k_1)}\right)^H a_n^{(k_2)}\left(\widehat{\boldsymbol{\xi}}_n^{(k_1)}\right)^H\widehat{\boldsymbol{\xi}}_n^{(k_2)}\right](\mathsf{x})\right\} \tag{4.18}$$

$$= \pi f_n \sum_{k=1}^{3}\left[\lambda_n^{(k)}\left(\widehat{\boldsymbol{\xi}}_n^{(k)}\right)^H\widehat{\boldsymbol{\xi}}_n^{(k)}\right](\mathsf{x}) = \sum_{k=1}^{3}\widehat{\boldsymbol{K}}_n^{(k)}(\mathsf{x}). \tag{4.19}$$

The simplification from (4.18) to (4.19) follows from the mutual uncorrelatedness of the SPOD coefficients shown in (4.12). Following the canonical treatment of VL (Landau & Lifshitz 1987), the total spectral VL can be decomposed into shear (deviatoric) and dilatational (compressible) contributions by separating the terms of the viscous stress tensor in (2.4) into its symmetric and divergence-related parts. In particular, we focus on the shear-driven contribution associated with the symmetric strain-rate tensor

$$\widehat{\boldsymbol{D}}_n(\mathsf{x}) \approx \mathrm{E}\left\{\left[\widehat{\mathsf{T}}_n : \nabla\widehat{\mathsf{y}}_n\right](\mathsf{x})\right\} \approx \mathrm{E}\left\{\left[\left(\sum_{k=1}^{3} a_n^{(k)}\widehat{\boldsymbol{T}}_n^{(k)}\right) : \nabla\left(\sum_{k=1}^{3} a_n^{(k)}\widehat{\boldsymbol{\xi}}_n^{(k)}\right)\right](\mathsf{x})\right\} \tag{4.20}$$

$$= \sum_{k=1}^{3}\lambda_n^{(k)}\left[\widehat{\boldsymbol{T}}_n^{(k)} : \nabla\widehat{\boldsymbol{\xi}}_n^{(k)}\right](\mathsf{x}) = \sum_{k=1}^{3}\widehat{\boldsymbol{D}}_n^{(k)}(\mathsf{x}). \tag{4.21}$$

which represents dissipation associated with strain rates. Here, $\widehat{\boldsymbol{D}}_n^{(k)}$ and $\widehat{\boldsymbol{D}}_n$ are effectively real with negligible imaginary components. The compressible term depends on the dilatation, $\nabla\cdot\hat{\mathsf{u}}$, and associated density gradient, $\nabla\beta$, which together represent volumetric and pressure-related damping. As shown in figure 36 in Appendix E, the compressible term contributes less than 1 % to the total, and can be reasonably neglected in the present analysis.

The rank-k spectral KE and VL fields take the forms of

$$\widehat{\boldsymbol{K}}_n^{(k)}(\mathsf{x}) = \pi f_n\lambda_n^{(k)}\left[\left(\widehat{\boldsymbol{\xi}}_n^{(k)}\right)^H\widehat{\boldsymbol{\xi}}_n^{(k)}\right](\mathsf{x}) \quad \text{and} \quad \widehat{\boldsymbol{D}}_n^{(k)}(\mathsf{x}) = \lambda_n^{(k)}\left[\widehat{\boldsymbol{T}}_n^{(k)} : \nabla\widehat{\boldsymbol{\xi}}_n^{(k)}\right](\mathsf{x}), \tag{4.22}$$

respectively. Their respective integral measures within the computational domain are

$$\widehat{K}_n^{(k)} = \sum_{\Omega} \widehat{\boldsymbol{K}}_n^{(k)}(\mathsf{x}) \Delta_x \Delta_y = \pi f_n \lambda_n^{(k)}, \quad \text{and} \quad \widehat{D}_n^{(k)} = \sum_{\Omega} \widehat{\boldsymbol{D}}_n^{(k)}(\mathsf{x}) \Delta_x \Delta_y, \tag{4.23}$$

where the normality of SPOD modes in (4.10) is used. Summing the contributions from the first three ranks yields

$$\widehat{K}_n = \sum_{\Omega} \widehat{\boldsymbol{K}}_n(\mathsf{x}) \Delta_x \Delta_y = \pi f_n \left(\lambda_n^{(1)} + \lambda_n^{(2)} + \lambda_n^{(3)} \right), \quad \text{and} \quad \widehat{D}_n = \sum_{\Omega} \widehat{\boldsymbol{D}}_n(\mathsf{x}) \Delta_x \Delta_y. \tag{4.24}$$

We approximate the integration over the discrete frequency f_n up to the Nyquist frequency using the summation operator

$$\mathcal{S}(\,\cdot\,) = \sum_{f_n \in (0, 1/(2\Delta t_{spod})]} (\,\cdot\,)\, \Delta f_n, \tag{4.25}$$

where $\Delta f_n = 1/(N_{DFT} \Delta t_{spod})$ is the frequency-bin width. In practice, the sum is evaluated using the trapezoidal rule. The rank-k contributions, obtained by integrating over the frequency domain, are defined as

$$\widehat{\mathcal{K}}^{(k)} = \mathcal{S}(\widehat{K}_n^{(k)}), \quad \text{and} \quad \widehat{\mathcal{D}}^{(k)} = \mathcal{S}(\widehat{D}_n^{(k)}), \tag{4.26}$$

respectively. Likewise, the corresponding total (all-rank) contributions are

$$\mathcal{K} = \mathcal{S}(\widehat{K}_n), \quad \text{and} \quad \mathcal{D} = \mathcal{S}(\widehat{D}_n). \tag{4.27}$$

From Parseval's theorem, the spectral integral of the viscous-loss density, $\mathcal{D}$, recovers the mean irreversible dissipation power, $\overline{D}$. The integrated frequency-weighted KE is a power-like spectral moment satisfying $\mathcal{K} = \overline{K}\,\overline{\omega}_k$, where $\overline{K}$ is the mean KE and $\overline{\omega}_k$ is the energy-weighted characteristic angular frequency. In general, $\mathcal{K}$ provides a convenient rate scale for comparison with $\mathcal{D}$ but does not, by itself, imply closure of the spectral KE budget. In the present study, the KE spectrum is strongly concentrated around the vortex-shedding frequency such that $\overline{\omega}_k$ is dominated by that peak, making $\mathcal{K}$ an effective single-time-scale measure of the KE dynamics. This interpretation is consistent with the metric used by Tam *et al.* (2001), which quantifies cycle-based energy conversion by averaging the KE of large-scale shedding vortices over an acoustic period.

Consistent with this representative case of $ISPL = 150\,\text{dB}$, $St = 4St_0$ analysed in figure 14, figure 21 presents the corresponding spectral KE and VL spectra, computed from the contributions of the first three leading SPOD modes. Within the analysis domain Ω, incident acoustic energy is primarily damped by conversion into KE of the induced flow fluctuations and irreversible viscous attenuation (Tam *et al.* 2001). We quantify these contributions using the spectral KE and VL components and define the total mode-frequency-resolved contribution as

$$\widehat{\boldsymbol{P}}_n^{(k)}(\mathsf{x}) = \widehat{\boldsymbol{K}}_n^{(k)}(\mathsf{x}) + \widehat{\boldsymbol{D}}_n^{(k)}(\mathsf{x}), \quad \widehat{P}_n^{(k)} \equiv \widehat{K}_n^{(k)} + \widehat{D}_n^{(k)} \quad \text{and} \quad \mathcal{P} \equiv \mathcal{K} + \mathcal{D}. \tag{4.28}$$

Here, $\widehat{\boldsymbol{P}}_n^{(k)}$ provides an estimate of the total spectral density of acoustic energy dissipation for mode k, combining energy stored in coherent vortical motion and energy irreversibly converted to heat through viscosity. In this representative case, the $\widehat{D}_n$ is roughly 20 % of $\widehat{K}_n$, indicating that most of the incident acoustic energy loss results from conversion into KE. In contrast, VLs still make a non-negligible contribution.

Figure 21(b) shows the spectral KE and VL fields associated with the fundamental frequency, 2nd harmonic frequency and spectral integration, respectively. At the

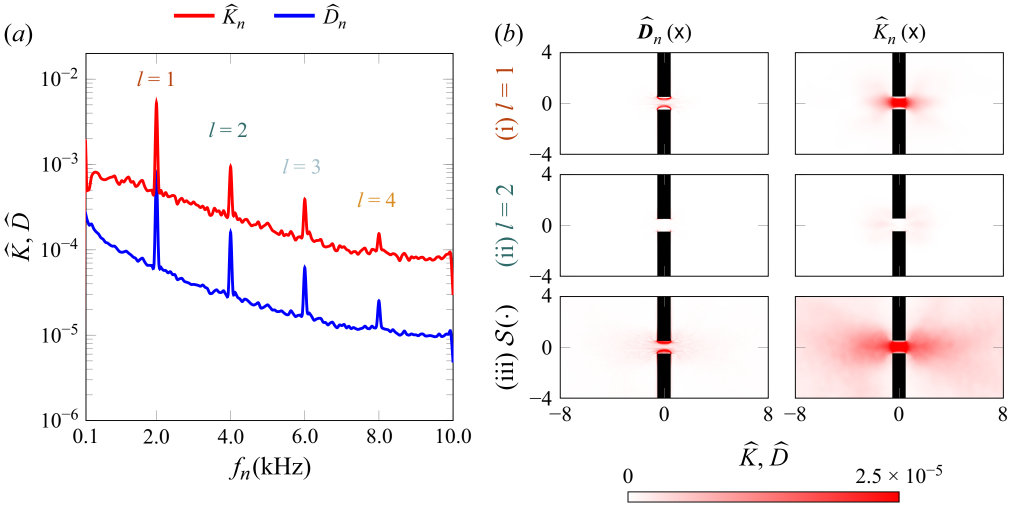

Figure 21. Acoustic energy dissipation at $ISPL = 150$ dB, $St = 4St_0$ and $Re = Re_0$: (*a*) energy dissipation spectra; and (*b*) spectral VL and frequency-weighted KE fields at harmonic indices $l = 1$ (*i*) and $l = 2$ (*ii*), together with the field as $\mathcal{S}(\widehat{\boldsymbol{D}}_n)(\mathsf{x})$ for VL and $\mathcal{S}(\widehat{\boldsymbol{K}}_n)(\mathsf{x})$ for KE contributions of all spectral components (*iii*).

fundamental frequency, both the spectral VL and KE fields show dominant structures, with the VL field concentrated within the slit and the KE field extending slightly outside the slit opening. At the second harmonic, the spectral VL field is localised near the slit corners. Due to the higher frequency, the associated vorticity exhibits reduced coherence. The vorticity cannot be convected as easily into the central region of the slit, resulting in concentrated dissipation at the slit periphery. This localisation is consistent with the reduced propagation distance of high-frequency vortical structures. The spectral KE field at the second harmonic is primarily located outside the slit, with its magnitude approximately 25 % that at the fundamental frequency. The limited spatial extent and energy content of this mode suggest that the KE is dissipated before forming large-scale coherent structures, which aligns with the localised dissipation observed in the spectral VL field. The overall VL field, $\mathcal{S}(\widehat{\boldsymbol{D}}_n)(\mathsf{x})$, remains confined to the slit region, reinforcing the role of boundary-layer interactions as the dominant mechanism of viscous energy losses. In contrast, the overall KE field, $\mathcal{S}(\widehat{\boldsymbol{K}}_n)(\mathsf{x})$, is more broadly distributed across the domain, with significant upstream and downstream structures.

To confirm the role of the boundary layer in viscous dissipation, figure 22 shows the normalised x-direction velocity profiles of the fundamental mode within the slit. These profiles are used to assess the spatial alignment between regions of maximum velocity gradients and maximum VL. The profiles exhibit a Poiseuille-like core in the central region of the slit, primarily driven by the pressure gradient between the upstream and downstream sides of the slit. This pressure difference also reflects the energy losses of the acoustic waves as they propagate through the slit. Near the walls, the profiles show velocity sign reversal, indicative of a pressure gradient reversal and consistent with the strong boundary-layer dissipation observed in the spectral VL field. Near the walls, and in particular at the slit corners, the profiles deviate from the Stokes-layer solution for channel flow, demonstrating that corner detachment is distinct from the simple phase reversal of an oscillating Stokes layer driven by the alternating acoustic pressure gradient. It is instead associated with a transient reversal of the wall shear stress and a localised flow detachment at the slit corner. The steepest velocity gradients occur within these

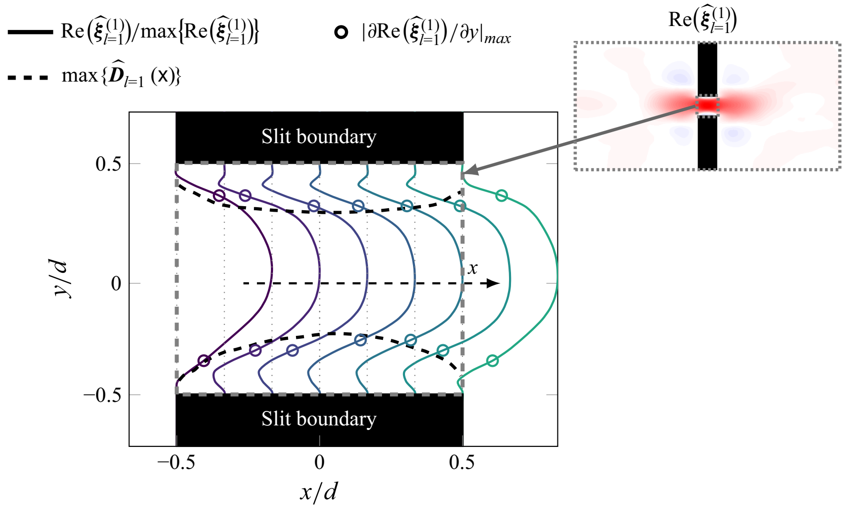

Figure 22. Profiles of the x-directional components, u, of the real component of the leading SPOD modes at the fundamental frequency, $\mathrm{Re}(\widehat{\boldsymbol{\xi}}^{(1)}_{l=1}/\max\{\widehat{\boldsymbol{\xi}}^{(1)}_{l=1}\})$, within the slit for $ISPL = 150$ dB, $St = 4St_0$ and $Re = Re_0$. The maximum mode gradient in y direction on the top and bottom halves of each profile, $|\partial \mathrm{Re}(\widehat{\boldsymbol{\xi}}^{(1)}_{l=1})/\partial y|_{max}$, is marked as a hollow circle. The maximum mode gradient aligns the maximum VL at the fundamental frequency observed in figure 21, using $\widehat{\boldsymbol{D}}_{l=1}(\mathsf{x})$.

boundary-layer zones, where the interaction between the oscillatory motion and the no-slip boundary condition generates intense shear. This large boundary-layer zone results in a thicker and more asymmetric dissipation field, consistent with previously discussed modal asymmetries. The spectral VL field is concentrated within the oscillatory boundary layer, aligning with regions where the y-direction gradient of the x-direction velocity, $\partial u/\partial y$, is maximum. This alignment confirms that the boundary-layer dynamics is responsible for viscous energy losses.

Figure 23 displays the KE and VL spectra, quantified via spatial integration, across the parameter space, illustrating the dependence of energy production and viscous dissipation on St, and Re at a fixed input sound pressure level of $ISPL = 150$ dB. As Re decreases, the VL in the broadband region becomes comparable to the KE rate, and the difference in peak magnitude between KE and VL also diminishes. At higher St, the VL spectrum even exceeds the KE spectrum at certain frequencies. This trend is consistent with the inverse proportional relation $\widehat{D}_n \propto 1/Re$, indicating that lower Reynolds numbers suppress irregular activity and reduce the relative contribution of broadband energy dissipation.

At higher St, the spectra are dominated by tonal peaks. When $St/St_0 > 4$, the peak amplitudes in both KE and VL spectra exceed the broadband levels by at least two orders of magnitude, suggesting minimal presence of irregular fluctuations. In the extreme case of $Re/Re_0 = 1/3$ and $St/St_0 = 12$, the tonal peak surpasses the broadband level by over six orders of magnitude. Conversely, the opposite extreme case of $Re/Re_0 = 1$ and $St/St_0 = 1$ shows a tonal-to-broadband contrast of less than one order of magnitude, indicating stronger irregular activity. These observations are consistent with the SPOD eigenvalue spectra, further confirming that increasing the slit thickness enhances viscous dissipation and leads to more pronounced tonal features. Additional KE and VL spectra at $ISPL = 150$ dB have similar features and are included in figure 33 in Appendix C.

For comparison, figure 24 displays the KE and VL spectra at $St/St_0 = 1$ and a lower input sound pressure level of $ISPL = 120$ dB, across varying Re. At this reduced acoustic

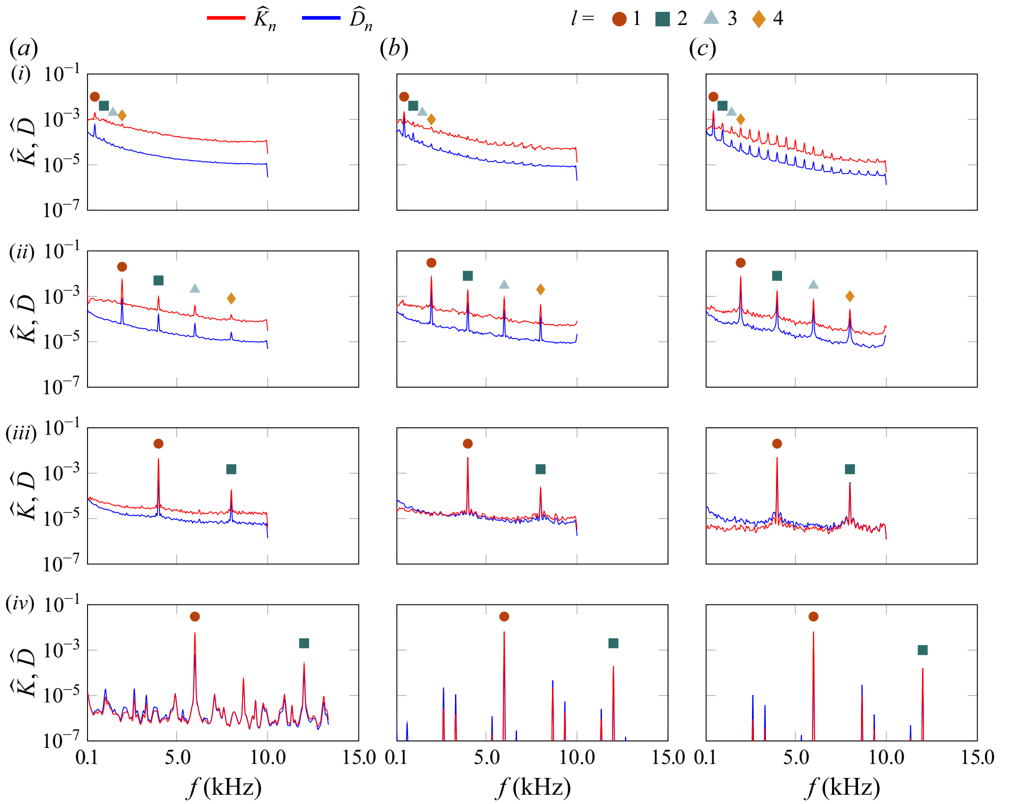

Figure 23. Frequency-weighted KE and VL spectra for different *St–Re* combinations at $ISPL = 150$ dB. The fundamental frequencies ($l = 1$) and their higher-order harmonics ($l \geq 2$) are manifested as distinct peaks in the spectra. Cases in column (*a*)–(*c*) represent $Re = Re_0$, $Re_0/2$ and $Re_0/3$. Cases in row (*i*)–(*iv*) represent $St = St_0$, $4St_0$, $8St_0$ and $12St_0$.

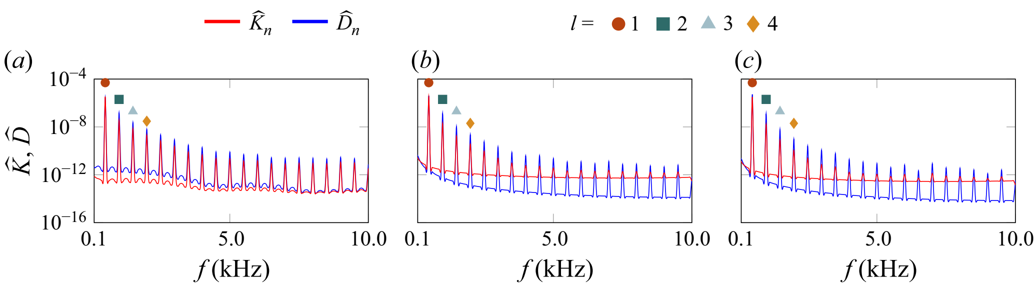

Figure 24. Frequency-weighted KE and VL spectra for different *Re* at $St = St_0$ and $ISPL = 120$ dB. The fundamental frequencies ($l = 1$) and their higher-order harmonics ($l \geq 2$) are manifested as distinct peaks in the spectra. Cases in column (*a*)–(*c*) represent $Re = Re_0$, $Re_0/2$ and $Re_0/3$.

forcing, the tonal peaks remain prominent, exceeding broadband levels by at least 4 orders of magnitude in both the KE and VL spectra. However, the overall energy levels are significantly diminished. The entire spectrum is approximately six orders of magnitude lower than that observed at $ISPL = 150$ dB, reflecting the strong dependence of both KE and viscous dissipation on the ISPL. Dissipation spectra for additional cases are provided in figure 35 in Appendix C.

https://doi.org/10.1017/jfm.2026.11896 Published online by Cambridge University Press

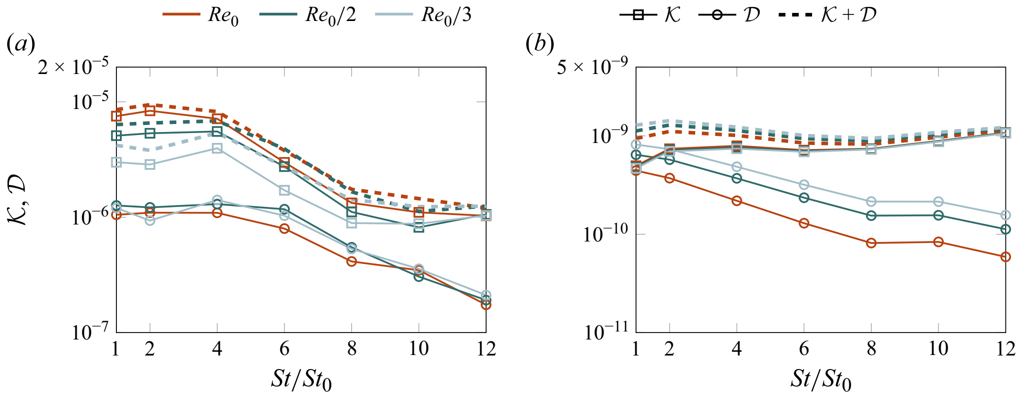

Figure 25. Overall KE, $\mathcal{K}$, and VL, $\mathcal{D}$, components, obtained by integrating over all frequency components via $\mathcal{S}(\,\cdot\,)$, across *St*–*Re* combinations for (*a*) $ISPL = 150$ dB and (*b*) $ISPL = 120$ dB.

Figure 25 shows the overall KE and VL obtained by summing the contributions from all frequency components and retaining only the first three leading SPOD modes, across the entire parameter space. At a higher sound pressure level of $ISPL = 150$ dB, the total VL accounts for approximately 20 %–60 % of the total KE. The combined total energy, $\mathcal{P} = \mathcal{K} + \mathcal{D}$, exhibits a three-stage trend that aligns with the absorption coefficient shown in figure 8. At low *St*, the total energy shows little sensitivity to *Re*. For intermediate frequencies, $4 \le St/St_0 < 10$, $\mathcal{P}$ increases monotonically with *Re*. At higher frequencies, $10 \le St/St_0 \le 12$, the total spectral energy is nearly independent of *Re*, indicating that Reynolds number effects become negligible in this regime because of the absence of significant broadband components. Among the cases, $Re = Re_0$ consistently yields the highest total energy conversion across the full range of acoustic frequencies, indicating the strongest energy dissipation mechanism. At a lower sound pressure level $ISPL = 120$ dB, VL plays a more significant role in the overall dissipation mechanism, ranging from approximately 20 %–180 % of the KE contribution. The *St*- and *Re*-dependence of the spectral KE is weaker than in the higher-amplitude cases, indicating reduced conversion of incident acoustic energy into vortical motion at lower forcing levels. In contrast, for smaller *Re*, VL is larger, highlighting the growing importance of direct viscous attenuation at low ISPL.

The trend of the total energy conversion is consistent with the absorption coefficient shown in figure 8. A fully closed comparison between the SPOD-based acoustic dissipation $\mathcal{P} = \mathcal{D} + \mathcal{K}$ and the far-field acoustic power absorption inferred from the three-microphone method would require evaluating the SPOD over a control volume that includes all boundary flux terms. Performing this full control-volume closure is left for future work.

Figure 26 recasts the integrated KE and VL against the in-slit Strouhal number. At 150 dB, $\mathcal{K}$ and the total $\mathcal{K} + \mathcal{D}$ are largest at small $St_{slit} \lesssim 0.2$, where vortex roll-up is strongest, and decline toward $St_{slit} = 1$, while $\mathcal{D}$ decreases monotonically; $Re = Re_0$ gives the largest conversion throughout. At 120 dB, the energies are several orders of magnitude smaller, $\mathcal{D}$ carries a larger share, and the *Re* ordering is clear across the St_{slit} range. The mode-resolved dissipation is thus described in the same in-slit variables as the impedance and absorption.

Together, these results provide a unified picture for interpreting dissipation mechanisms in acoustic slit flows, specifically those associated with slit-resonator mouths. At low *St* and low ISPL, the incident acoustic energy loss receives comparable contributions

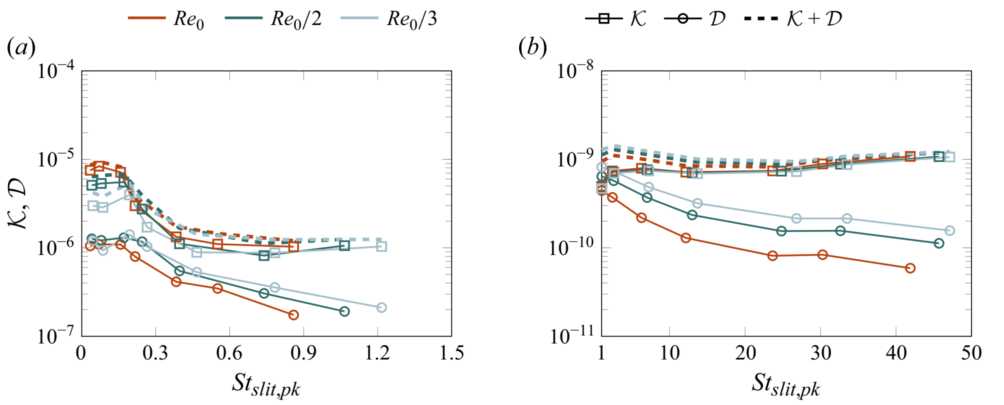

Figure 26. Overall KE, $\mathcal{K}$, and VL, $\mathcal{D}$, as in figure 25 but plotted against the in-slit Strouhal number $St_{slit,pk}$, for (*a*) $ISPL = 150$ dB and (*b*) 120 dB.

from the KE of the induced flow field and spatially distributed VL. For larger St and $ISPL$, the dissipation becomes more localised near the slit mouth, and the KE associated with shed vortices comes to dominate the acoustic damping mechanism. This evolving balance between viscous and vortex-driven dissipation mechanisms underlies the nonlinear acoustic damping observed in slit openings at high ISPL, governing energy-transfer efficiency and damping performance.

4.6. *The ISPL dependence*

In addition to the two baseline forcing levels, $ISPL = 120$ and 150 dB, two intermediate levels, $ISPL = 140$ and 145 dB, are considered to assess the dependence on acoustic amplitude. Figure 27 shows the leading SPOD mode in the four ISPL cases considered, for a representative acoustic excitation with $St = 2St_0$ and $Re = Re_0/3$. The corresponding slit Reynolds numbers are $Re_{slit} = 33$, 325, 588 and 1008 at $ISPL = 120$, 140, 145 and 150 dB, respectively. At $ISPL = 120$ dB, the leading mode remains spatially confined to the vicinity of the slit. As ISPL increases beyond 140 dB, the leading mode indicates the onset of vortex shedding, with an increasing characteristic length scale and a progressively larger spatial extent in the near-slit region. These results suggest a transition in the in- and near-slit flow dynamics towards progressively stronger inertial effects and more spatially extended coherent shedding structures.

Figure 28 compares the frequency-weighted VL and KE spectra for different ISPL values for $Re = Re_0/3$ at $St = 2St_0$. For this particular case, KE dominates acoustic dissipation across all ISPL values. In contrast, the relative contributions of these two dissipation pathways vary under different acoustic forcing excitations, as shown in figure 25. The tonal peaks in both VL and KE increase monotonically with ISPL, indicating stronger acoustic absorption at higher forcing amplitudes. These trends are consistent with the expectation that larger pressure gradients and higher local inertia relative to viscosity promote a stronger shear-layer dynamics over an acoustic cycle (Shuster & Smith 2007). The separation of SPOD eigenvalues across ISPL values across the spectrum further suggests that higher ISPL is associated with an increase in the broadband contribution. In addition, the relative contrast between tonal peaks and broadband components is markedly reduced at the highest forcing level, 150 dB. This observation indicates that, in addition to the coherent vortical motion and its higher-order

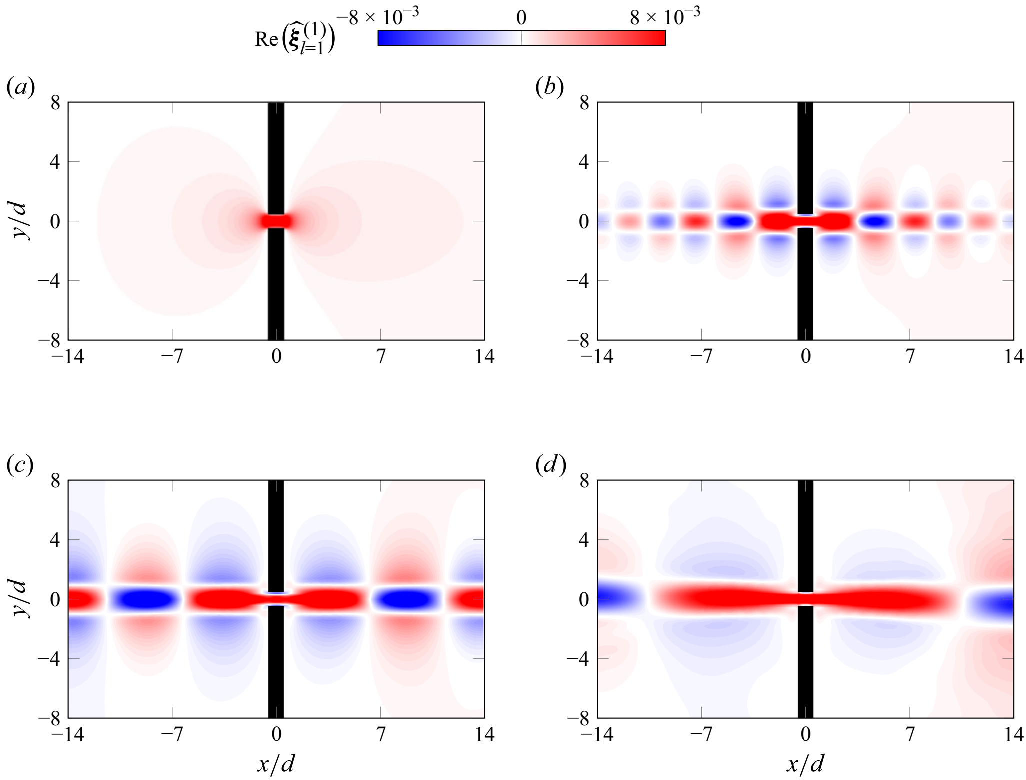

Figure 27. Leading SPOD modes, Re$(\widehat{\boldsymbol{\xi}}^{(1)}_{l=1})$, for different *ISPL* at $St = 2St_0$ and $Re = Re_0/3$. Cases in (*a*)–(*d*) represent $ISPL = 120$, 140, 145 and 150 dB, respectively.

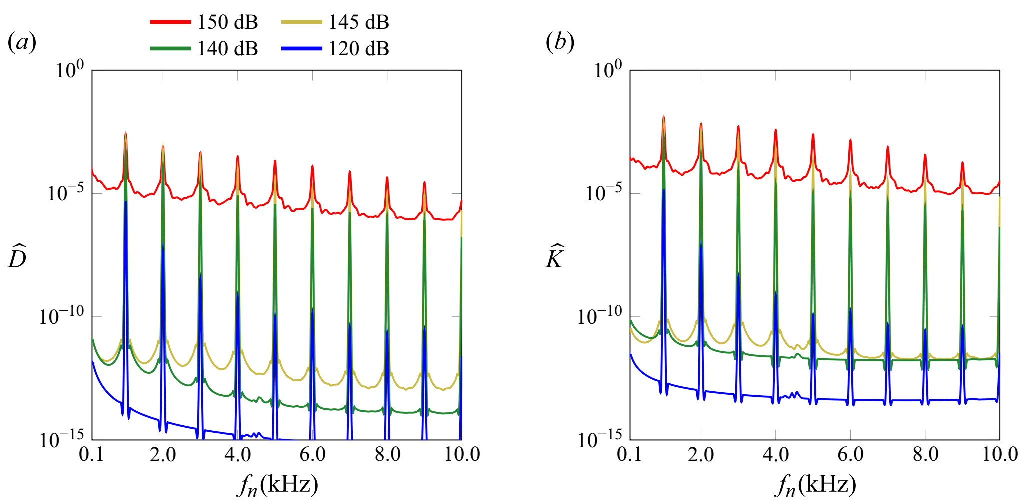

Figure 28. Frequency-weighted VL (*a*) and KE (*b*) spectra for different *ISPL* at $Re = Re_0/3$ at $St = 2St_0$.

harmonics, the irregular nonlinear dynamics makes an increasingly important contribution at high acoustic amplitude.

5. Discussion

We use SPOD to disentangle the energy contributions, KE and VL, in an acoustically driven slit configuration for various frequencies. We directly link the contributions to their corresponding coherent spatial structures. This spectral analysis view reveals rich and distinct dissipation behaviours across the parameter space. The overall VL at $ISPL = 150$ dB remains high, reaches its maximum near $St = 4St_0$ and then drops by approximately 50 % for $St \geq 6St_0$. At this ISPL, dissipation is primarily driven by the conversion of incident acoustic energy into KE. We interpret the St-dependence of this behaviour through the Keulegan–Carpenter number, $K_c = 2\pi/St_{slit}$. For $ISPL = 150$ dB with $\widehat{A} \approx 894$ Pa, the peak velocity measured in the slit, shown in table 2, is an order of magnitude larger than the far-field approximation based on the incident particle velocity. For $St = 4St_0$, the peak velocity gives $u_{slit,pk} = 63.8$m/s and $K_c = 39.88$. The parameter K_c describes the velocity amplitude in terms of 40 times the slit thickness. That is, fluid particles traverse the entire slit width during each oscillation cycle. This small K_c promotes shear layer near the mouth of the slit, consistent with the large velocity gradients shown in figure 18, and results in the viscous attenuation of acoustic energy.

For $St > 4St_0$, the induced flow organises into more confined, X-shaped SPOD modes, as observed in figure 17, with reduced viscous dissipation. Previous studies have observed similar results in relevant physical configurations. Viscous dissipation was found to degrade the performance of sound-driven jet pumps with the onset of corner vortex propagation from the appearance of periodic peaks, occurring around $K_c > 0.7$ (Oosterhuis *et al.* 2017) and $K_c \approx 1.3$ (Timmer *et al.* 2016). Likewise, Sarpkaya (1986) reported a maximum drag coefficient for a circular cylinder in oscillatory flow at $K_c \approx 1$ and $Re = 11240$. At the lower sound pressure level of $ISPL = 120$ dB, dissipation is instead dominated by VL, and the overall KE shows a much weaker dependence on St compared with $ISPL = 150$ dB. For all cases at this ISPL, the small K_c indicates that particle displacements are much smaller than the slit thickness, and vortex roll-up is suppressed. As a result, for larger St, the overall VL is smaller, consistent with weaker shear-driven dissipation in the boundary layers.

We observe that tonal peaks emerge at non-harmonic frequencies with high St, particularly at lower Re. The appearance of this spectral branching and the associated non-harmonic peaks indicates that nonlinear triadic interactions play an important role in redistributing energy across frequencies at large St. These interactions introduce additional dissipation pathways and are thus important to understand for optimal slit design. However, such a dynamics cannot be directly predicted by linear theory or by linear-based modal-decomposition techniques such as POD, DMD or SPOD, due to their inherently nonlinear nature. In the present work, SPOD-based spectral analysis statistically isolates dominant coherent structures from the broadband response but does not resolve the mechanisms governing inter-frequency energy transfer. To identify the optimal coherent structures participating in triadic interactions and to quantify the associated energy budgets among these triadic modes, the recently proposed triadic orthogonal decomposition (TOD) by Yeung *et al.* (2026) offers a promising path forward. By construction, TOD identifies coherent flow structures that optimally represent spectral momentum transfer, quantifies their coupling and energy exchange through an energy-budget bispectrum and localises the regions where these interactions occur. This analysis is well suited to regimes in which spectral peaks occur at non-integer multiples of the forcing frequency.

The observed dissipation mechanism has several implications for slit-resonator design, whether the application calls for high or low damping. Beyond conventional design based solely on the resonant frequency, energy dissipation can be enhanced by tailoring the slit-mouth thickness to deliberately scale *St*, *Re* and K_c, thereby maximising VL in the desired operating range. The dependence of the dissipation on K_c recovers the established picture based on Strouhal number (e.g. Ingard & Labate (1950) and Aulitto (2023)). In particular, large-K_c operation at high ISPL promotes strong vortex roll-up and efficient shear-driven attenuation, whereas lower-K_c regimes favour more linear, viscosity-dominated damping with reduced sensitivity to broadband fluctuations. The present spectral analysis adds to this picture by resolving the spatial and spectral partition between the KE and VL channels, thereby refining qualitative regime trends into more specific design guidance. The VL field is governed primarily by the geometry of the mouth region, where the oscillatory shear layer forms and more than 99 % of the loss is concentrated within a few slit widths of the opening. This modal structure indicates that the slit-mouth geometry, and in particular the slit width, directly controls the viscous damping contribution. The KE field, by contrast, extends several slit widths beyond the slit mouth on both sides. This spatial distribution suggests that a design can further exploit the external region where shed vortices carry KE away from the opening. For example, a secondary element, such as an additional slit or neighbouring resonant feature, could be positioned to intercept and dissipate this convected energy rather than allowing it to leave the near-slit region. The mode-resolved fields thus separate two distinct design directions: the in-slit wall region for VL, and the external KE distribution that determines the spatial range and strength of energy exchange away from the slit mouth. These findings suggest practical guidelines for the design of acoustic liners and metasurfaces for applications such as duct acoustics and noise-control devices, where robust, broadband and amplitude-tolerant damping is required. By explicitly accounting for the coupled roles of *St*, *Re*, ISPL and K_c, we can engineer slit resonators and related subwavelength elements for optimal impedance at a target frequency. They can also be designed for controlled nonlinear damping characteristics under realistic high-amplitude operating conditions.

The present study focuses on a simplified slit with anechoic termination, rather than a full slit resonator. While both systems share the same fundamental mechanism of acoustic–vorticity conversion at the slit mouth, only the resonator can support standing-wave resonance for $f_s \leq 6$ kHz due to its reflective hard termination. The simplified slit configuration isolates local generation and dissipation of vortices at the slit mouth, enabling the examination of energy-transfer mechanisms without contamination from global resonant modes. This strategy is canonical: first analysing elementary configurations, then addressing fully coupled resonant systems. Accordingly, the present work can be viewed as a first step toward a complete characterisation of nonlinear acoustic damping in slit resonators. The acoustically driven slit without a cavity is also relevant beyond slit resonators, including the classical half-wave resonator at high frequencies. An anechoically terminated configuration is therefore useful for element-level characterisation of such applications, including air leaks, perforate-type elements and nozzles, for which the reflection from the termination may be weak and application-dependent. In a companion study (in preparation), the analysis will be extended to true resonator configurations with hard terminations and discrete resonance frequencies.

6. Conclusion

This study develops rigorous numerical and spectral analyses to quantify the conversion of incident acoustic energy into coherent, energy-ranked KE and VL in a thin, large-aspect-ratio slit. Two-dimensional DNSs are performed over a broad imposed parameter space in Strouhal number (*St*), Reynolds number (*Re*) and sound level (ISPL), yielding a dataset spanning the linear to strongly nonlinear flow regimes. These imposed acoustic parameters are then related to the induced near-slit flow parameters that govern vortex formation and the associated nonlinear flow regimes. Three-dimensional simulations further demonstrate that the dominant flow physics are captured effectively within a 2-D model. Rather than characterising only the net acoustic energy dissipation via power absorption coefficients, SPOD is used to separate and quantify, mode by mode, the contributions of KE and VL at each frequency. For each spectral component, the associated KE and VL mechanisms are linked to their coherent spatial structures, revealing robust, physically interpretable processes that govern nonlinear acoustic dissipation within and near slit-type openings. This analysis reveals that acoustic–KE–VL energy exchange at the slit mouth is governed by the coupled effect of *St*, *Re* and ISPL. Their interplay controls not only the coherence and strength of vortex shedding but also the partitioning between spectral KE and VL, which ultimately determines the dissipation characteristics of the acoustic slit. The conventional, overall acoustic energy dissipation picture is recovered by summing the KE and VL contributions obtained from the SPOD modes, followed by spatial and spectral summations.

Across all *St*–*Re*–ISPL combinations, more than 99 % of the VL originates from the near-slit region (within the $16d \times 8d$ region shown in figure 21*b*). The leading SPOD rank at the fundamental frequency accounts for over 95 % of the total energy, so the induced flow field is low rank at the fundamental frequency. The corresponding dissipation field aligns with regions of maximum velocity gradient, confirming that incident acoustic energy loss is governed primarily by the boundary-layer dynamics and its nonlinear interactions with the slit geometry.

At $ISPL = 150\,\text{dB}$, the in-slit velocity ranges approximately 25–75 m s^{-1} across the parameter sweep, so fluid particles traverse many slit widths per oscillation cycle in all cases. In this regime, the largest integrated KE and VL occur near conditions at $St \leq 4St_0$ corresponding to Keulegan–Carpenter number $K_c \geq 40$, where the oscillatory boundary layer undergoes vortex roll-up at the slit corner, generating large-scale vortices that dominate the SPOD spectra and drive strong conversion of incident acoustic energy into KE and VL. For $St > 8St_0$, contraction of the oscillatory boundary layer suppresses vortex roll-up, yielding more confined, X-shaped modes and an associated $\sim 50\,\%$ reduction in dissipation, despite persistent harmonic content. At lower *St* (e.g. $St = St_0$), KE-dominated dissipation is less pronounced, and the *Re*-dependence of the modal structures becomes more evident. In this regime, the total VL increases monotonically with decreasing *Re*, indicating the growing dominance of direct viscous attenuation.

Case studies at $(St, Re) = (4St_0, Re_0/2)$ and $(8St_0, Re_0)$ show that increasing the slit thickness (i.e. increasing the Womersley number) produces more confined fundamental SPOD modes, sharper harmonic peaks and reduced broadband KE. This result demonstrates that thickness-selective design can induce dissipation changes comparable to those obtained by varying the Strouhal number, *St*. Increasing both the slit thickness and *St* tends to compress vortex-shedding structures toward the slit mouth, reshaping the balance between tonal and broadband dissipation.

Acknowledgements. The authors thank Professors K.K. Ahuja and L.N. Sankar for fruitful discussions. We acknowledge the referees' comments, which have helped improve the quality of our paper.

Funding. H.Y. acknowledges support from the Georgia Institute of Technology Small Bets Internal Research and Development (IRAD) Program. T.C. and S.H.B. acknowledge support from the U.S. Department of Defense, the Army Research Office under Grant No. W911NF-23-10324 (PMs Drs D. Ford and R. Martin).

Frequency (kHz)	Re ($Re_0 = 17746$)	$u_{slit,\,pk}$ (m/s) ($ISPL = 150$ dB)	Re_{slit} (150 dB)	$u_{slit,\,pk}$(m/s) ($ISPL = 120$ dB)	Re_{slit} (120 dB)
0.5	Re_0, $Re_0/2$, $Re_0/3$	73.1, 61.6, 55.9	3785, 1593, 965	2.49, 2.47, 2.49	129, 64, 43
1.0	Re_0, $Re_0/2$, $Re_0/3$	72.6, 63.4, 58.4	3756, 1640, 1008	2.07, 1.93, 1.91	107, 50, 33
2.0	Re_0, $Re_0/2$, $Re_0/3$	63.8, 58.9, 51.9	3300, 1523, 895	1.60, 1.43, 1.39	83, 37, 24
3.0	Re_0, $Re_0/2$, $Re_0/3$	69.7, 61.6, 56.9	3608, 1593, 981	1.24, 1.16, 1.10	64, 30, 19
4.0	Re_0, $Re_0/2$, $Re_0/3$	52.5, 50.7, 43.1	2715, 1313, 744	0.85, 0.81, 0.75	44, 21, 13
5.0	Re_0, $Re_0/2$, $Re_0/3$	45.6, 34.0, 32.1	2362, 879, 553	0.83, 0.77, 0.75	43, 20, 13
6.0	Re_0, $Re_0/2$, $Re_0/3$	35.1, 28.3, 24.8	1816, 732, 427	0.72, 0.66, 0.64	37, 17, 11

Table 2. Reynolds numbers based on two velocity scales. The nominal Reynolds number $Re_0 \equiv \rho c d/\mu$ is used to control viscosity in the simulations, while the slit Reynolds number $Re_{slit} \equiv \rho u_{slit,pk} d/\mu$ uses the peak velocity measured inside the slit, $u_{slit,pk} \equiv \max_t \max_{(x,y)\in\Omega_{slit}} |u(x, y, t)|$. For each source frequency, the table reports the Re_{slit} across the three viscosity levels and two ISPLs.

This work used NCSA Delta through allocation TG-PHY210084 (PI Bryngelson) from the Advanced Cyberinfrastructure Coordination Ecosystem: Services & Support (ACCESS) program, supported by National Science Foundation grants nos. 2138259, 2138286, 2138307, 2137603 and 2138296. We acknowledge the use of computational resources at Georgia Tech, including PACE Phoenix.

Declaration of interests. The authors declare that they have no known competing financial interests or personal relationships that could have appeared to influence the work reported in this paper.

Author contributions. **HY**: Conceptualisation, Formal analysis, Methodology, Software, Investigation, Data Curation, Validation, Visualisation, Writing – original draft, Writing – review and editing. **TC**: Conceptualisation, Formal analysis, Methodology, Software, Investigation, Validation, Visualisation, Supervision, Writing – original draft, Writing – review and editing. **SHB**: Conceptualisation, Funding acquisition, Methodology, Project administration, Resources, Supervision, Writing – original draft, Writing – review and editing.

Data availability statement. MFC is available in perpetuity under the MIT licence at https://github.com/MFlowCode/MFC. The database is permanently available in the Georgia Tech Digital Repository at https://doi.org/10.35090/gatech/80504 `this link` and this reference (Yu *et al.* 2025*b*).

Appendix A. In-slit velocity

The nominal Reynolds number $Re \equiv \rho co/\mu$ is used throughout to control viscosity in the simulations, consistent with our non-dimensionalisation. However, the characteristic velocity in the slit is neither the speed of sound nor the particle velocity of the source wave but the locally induced velocity caused by geometric contraction effects. To quantify how the effective Reynolds number varies with the imposed forcing amplitude, we therefore define an additional slit Reynolds number, Re_{slit}, based on the peak velocity within the slit, $u_{slit,\,pk}$

$$Re_{slit} \equiv \frac{\rho\, u_{slit,pk}\, o}{\mu}, \qquad u_{slit,pk} \equiv \max_t \max_{(x,y)\in\Omega_{slit}} |u(x, y, t)|. \tag{A1}$$

Table 2 reports Re_{slit} for all source frequencies, viscosity, and ISPLs. Slit Reynolds number increases with ISPL and also exhibits frequency dependence through the resulting in-slit velocity response. In particular, for $ISPL = 150$ dB, $Re_{slit} \sim O(10^3)$ across the parameter space, whereas for $ISPL = 120$ dB, Re_{slit} drops to $O(10^1)$–$O(10^2)$. Changing ISPL and frequency moves the system between substantially different effective Reynolds numbers within the slit, providing a more physically interpretable basis for comparing vortex formation, coherent structures, and VL across cases.

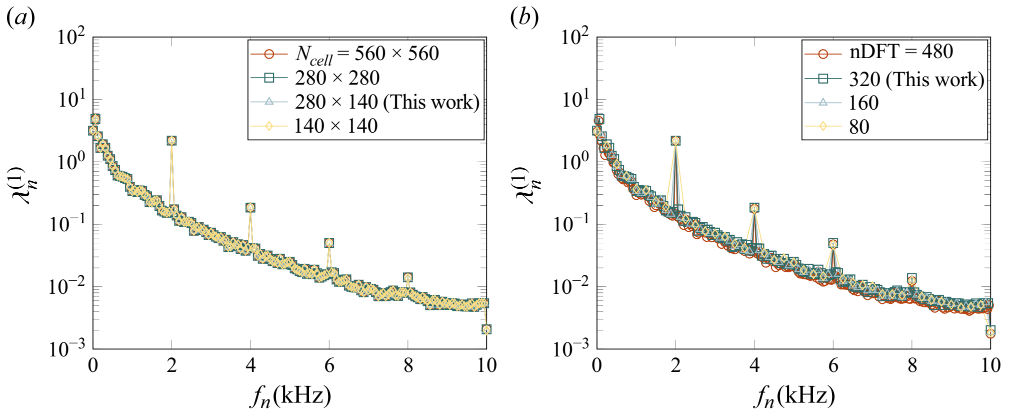

Figure 29. Convergence of the SPOD eigenvalue spectra $\lambda_n^{(1)}$ with (*a*) spatial resolution convergence with variation in the number of grid cells N_{cell} used to construct the snapshot vector at fixed $n_{DFT} = 320$ and (*b*) block-length convergence with variation in the DFT block length n_{DFT}, at fixed $N_{cell} = 280 \times 140$. The eigenvalue of the leading SPOD mode is demonstrated. The SPOD configuration used in this work ($N_{cell} = 280 \times 140$, $n_{DFT} = 320$) is highlighted.

Appendix B. SPOD convergence

This appendix presents a convergence study of the SPOD analysis to justify the resolution and block-length parameters used in this study. We use the case at $ISPL = 150$ dB, $St = 4St_0$ and $Re = Re_0$ as a representative example and results for the other cases are similar.

Figure 29(*a*) shows the SPOD eigenvalue spectra computed from snapshot vectors of four different spatial resolutions, ranging from 140×140 to 560×560, with the temporal block length fixed (nDFT = 320). The leading mode eigenvalues are essentially indistinguishable across the four resolutions, indicating that the dominant coherent structures and their relative energy content are convergent with further spatial refinement. Therefore, the spatial resolution used in this work (280×140) provides converged SPOD modes. Figure 29(*b*) shows the corresponding spectra for four DFT block lengths nDFT = 80, 160, 320 and 480 with the spatial resolution fixed at $N_{cell} = 280 \times 140$. Increasing nDFT improves the frequency resolution and thus produce narrower tonal peaks but reduces the number of independent blocks, so an appropriate value must balance these two effects. For nDFT ≤ 160 the leading eigenvalue at the forcing frequency and its harmonics is slightly under-resolved, but for nDFT ≥ 320 the leading eigenvalue and the separation from the suboptimal branch become essentially independent of nDFT. Therefore, we use nDFT = 320 for all cases reported in this study, which provides adequate frequency resolution at the tonal peaks while retaining a sufficient number of blocks for statistical convergence.

Appendix C. Complementary instantaneous and spectral results

This appendix presents complementary instantaneous and spectral results for the low- and high-amplitude forcing cases, $ISPL = 120$ and 150 dB, respectively, supplementing the analyses in §§ 3 and 4. These results further illustrate the evolution of the modal structure, spectral energy distribution, and dissipation across the full parameter range considered.

C.1. *High ISPL*

Figure 30 shows the instantaneous vorticity fields from the present database for various *St*–*Re* combinations at $ISPL = 150$ dB. Consistent with the representative cases shown in figure 5, these snapshots exhibit well-resolved boundary layers generated by the interaction of the oscillatory flow with the slit, followed by the development of periodic vortex shedding. These results demonstrate that, over this parameter range, a portion of the incident acoustic energy is converted into vortical motion through its interaction with the 2-D slit.

Figure 31 displays the fundamental modes for $St = 2St_0$, $= 6St_0$, and $= 10St_0$ at $ISPL = 150$ dB. At $St = 2St_0$, the fundamental mode retains relatively large-scale structures. Similar to cases with $St \leq 4St_0$, the coherent structure extends outward from the slit further with *Re* reduced. At $St \geq 6St_0$, the fundamental modes exhibit X-shaped patterns near the slit, similar to cases at $St = 8St_0$ and $= 12St_0$.

Figure 32 displays the corresponding SPOD eigenvalues for the cases shown in figure 31. As *St* increases and *Re* decreases, the spectral peaks sharpen and the rank hierarchy becomes more distinct. The reduction of broadband energy with decreasing *Re* is also evident across all three *St*, consistent with the results observed in § 4.3 with lower *Re* flows.

Figure 33 displays the corresponding dissipation spectra of these cases. Across all three *St*, the spectral VL peaks are aligned with the peaks of the KE spectra, indicating that VLs remain closely tied to the vorticity dynamics of the dominant coherent mode. With larger *St* and smaller *Re*, the difference between the total KE and VL diminishes noticeably, consistent with reduced vorticity coherence and increased viscosity.

C.2. *Low ISPL*

Figure 34 displays the fundamental modes of these cases. For $St = St_0$, we observed dumbbell-shaped structures with thicker boundary layer near the slit wall. For $St = 2St_0$, the structure appears to be an intermediate shape between dumbbell-shaped and X-shaped, with barely distinguishable *Re*-dependence. When $St \geq 4St_0$, the modal structures look similar across different *Re*, indicating a negligible difference in the coherent vortical structure across the parameter space.

Figure 35 displays the dissipation spectra of these cases. The broadband spectral energy is at least five orders of magnitude smaller than the narrow tonal peaks across all the parameter space. The broadband contribution from the KE is negligible at this ISPL. Additional peaks at non-integer multiples of the forcing frequency appear at $St \geq 4St_0$, suggesting nonlinear interactions with the slit boundaries even at an *ISPL* as low as 120 dB.

Appendix D. Effects of slit opening

This appendix expands on the role of the slit opening as a length-scale coupling *St*, *Re*, and *Wo*, complementing the discussion in § 4.3. Doubling the characteristic length scale, o, in the case where $St_1 = 4St_0$ and $Re_1 = Re_0/2$ results in a new configuration with $St_2 = 8St_0$ and $Re_2 = Re_0$. Although this transformation does not strictly preserve dynamic similarity, it provides a metric for a parametric trajectory governed by the Womersley number, which is

$$Wo \equiv \frac{o}{2}\sqrt{\frac{2\pi f_s}{\nu}}. \tag{D1}$$

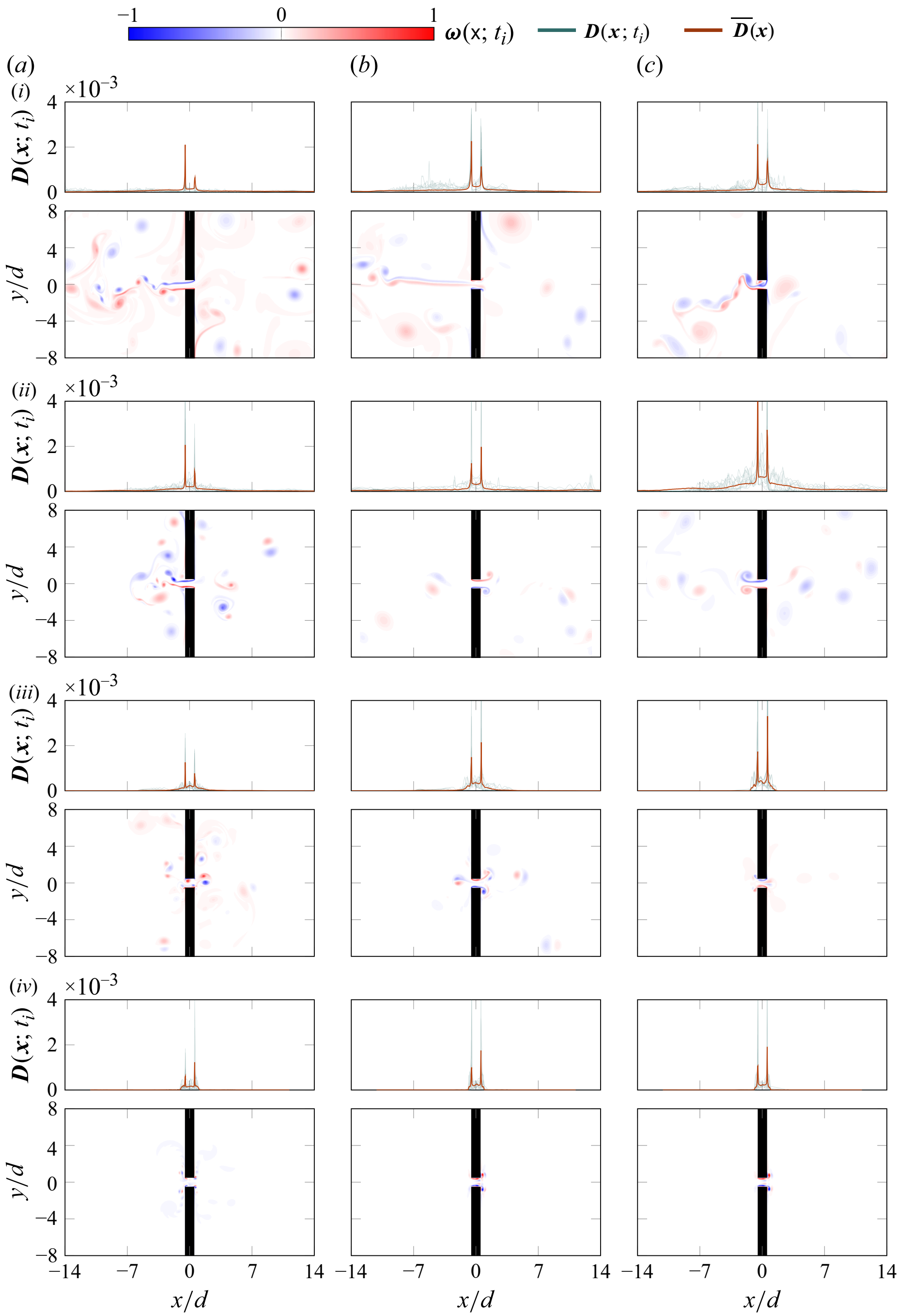

Figure 30. Instantaneous VL (integrated across the y direction), $\boldsymbol{D}(\boldsymbol{x};\, t_i)$, and vorticity fields, $\boldsymbol{\omega}(\mathrm{x};\, t_i)$, for different St–Re combinations at $ISPL = 150\,\mathrm{dB}$. Temporal-averaged VL fields, $\overline{\boldsymbol{D}}(\boldsymbol{x})$, are shown for comparison. Cases in column (a)–(c) represent $Re = Re_0$, $Re_0/2$, and $Re_0/3$. Cases in row (i)–(iv) represent $St = St_0$, $4St_0$, $8St_0$,and $12St_0$.

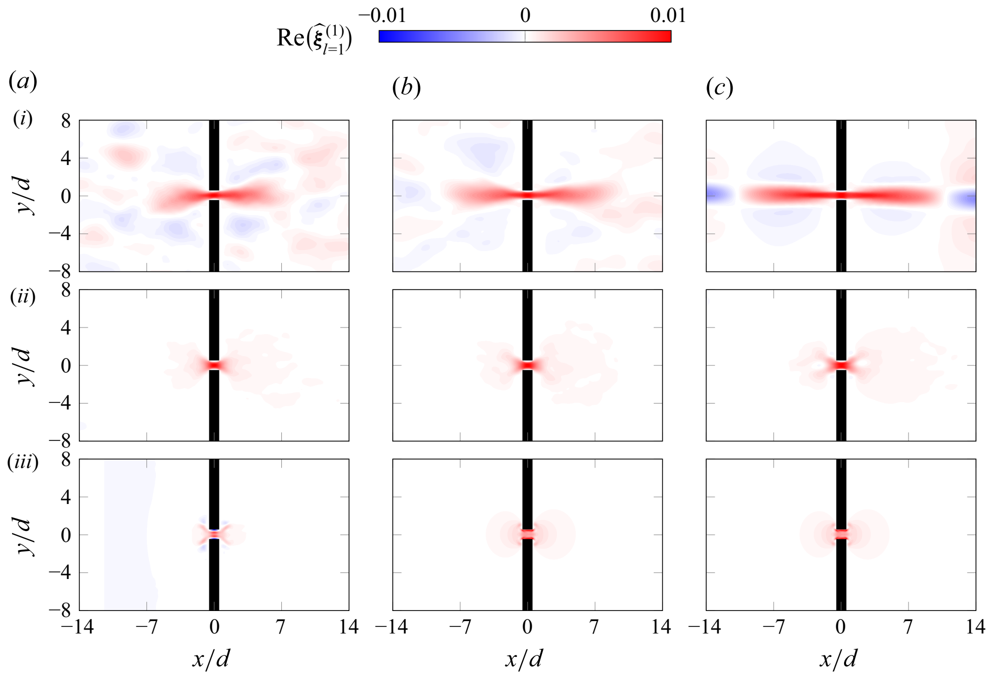

Figure 31. Leading SPOD modes, $\mathrm{Re}(\widehat{\boldsymbol{\xi}}^{(1)}_{l=1})$, for the complementary St–Re combinations at $ISPL = 150$ dB shown in figure 17, plotted at their respective fundamental frequencies ($l = 1$) as their x-directional components, u. Cases in column (*a*)–(*c*) represent $Re = Re_0$, $Re_0/2$ and $Re_0/3$. Cases in row (*i*)–(*iii*) represent $St = 2St_0$, $6St_0$ and $10St_0$.

The Womersley number, Wo, was introduced to characterise the relative importance of inertial and viscous forces in pulsatile pipe flows (Womersley 1955), and scales linearly with the characteristic length.

The geometric scaling among St, Re, and Wo can be expressed as

$$Wo \sim \sqrt{Re\,St} = \sqrt{(c\,o/\nu)\,(f_s\,o/c)} = o\sqrt{f_s/\nu}. \tag{D2}$$

Thus, doubling the slit opening (i.e. the effective length scale in this study) doubles Wo and results in a SPOD eigenvalue spectrum with more distinguishable peaks and weaker broadband levels. A similar trend is observed in the comparison between the cases with $St_1 = 4St_0$ and $Re_1 = Re_0/3$ and $St_2 = 12St_0$ and $Re_2 = Re_0$, where the latter corresponds to a tripling of the length scale. Additional cases supporting this observation, not shown in figure 16, are provided in figure 32 in Appendix C. This observation is conceptual, and we do not vary o in the DNS. In practical resonator designs, changes in slit opening alter St and Re through geometric changes, with an additional dependence on the properties of the background fluid.

Appendix E. Compressibility contribution of the dissipation

Figure 36 shows spectra of both contributions at the representative case demonstrated in § 4.2. The deviatoric contribution is two orders of magnitude larger than the compressible

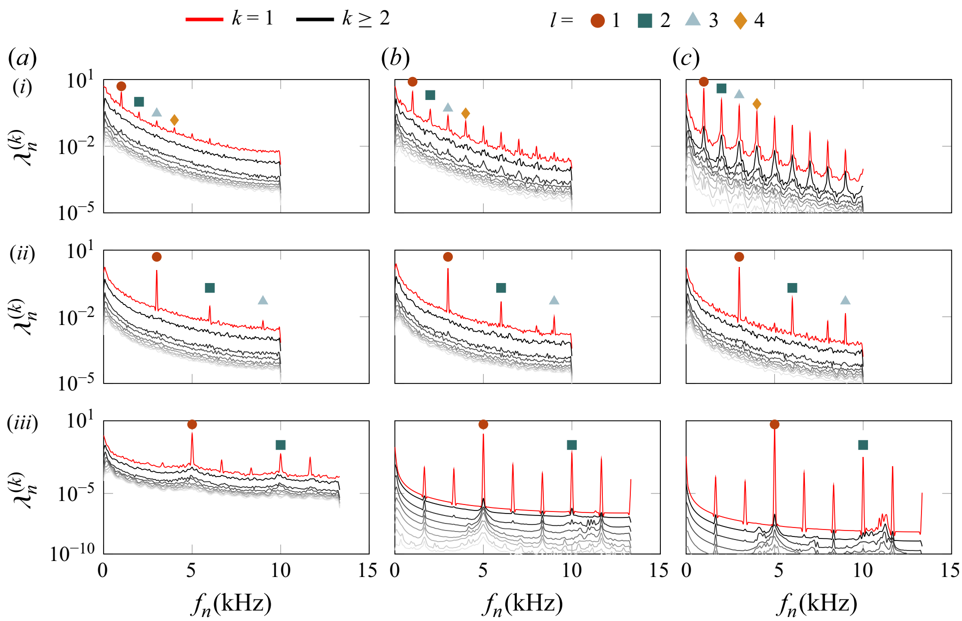

Figure 32. SPOD eigenvalue spectra, ${\lambda_n}^{(k)}$, at different rank k for the complementary *St*–*Re* combinations at $ISPL = 150$ dB shown in figure 16. Cases in column (*a*)–(*c*) represent $Re = Re_0$, $Re_0/2$ and $Re_0/3$. Cases in row (*i*)–(*iii*) represent $St = 2St_0$, $6St_0$ and $10St_0$. The fundamental frequency ($l = 1$ defined in (4.13)) and its higher-order harmonics ($l \geq 2$) manifest as distinct peaks in the spectrum. For example, two tonal peaks arise at $f_n = 5$ kHz ($l = 1$) and $f_n = 10$ kHz ($l = 2$) in case (*a*, *iii*).

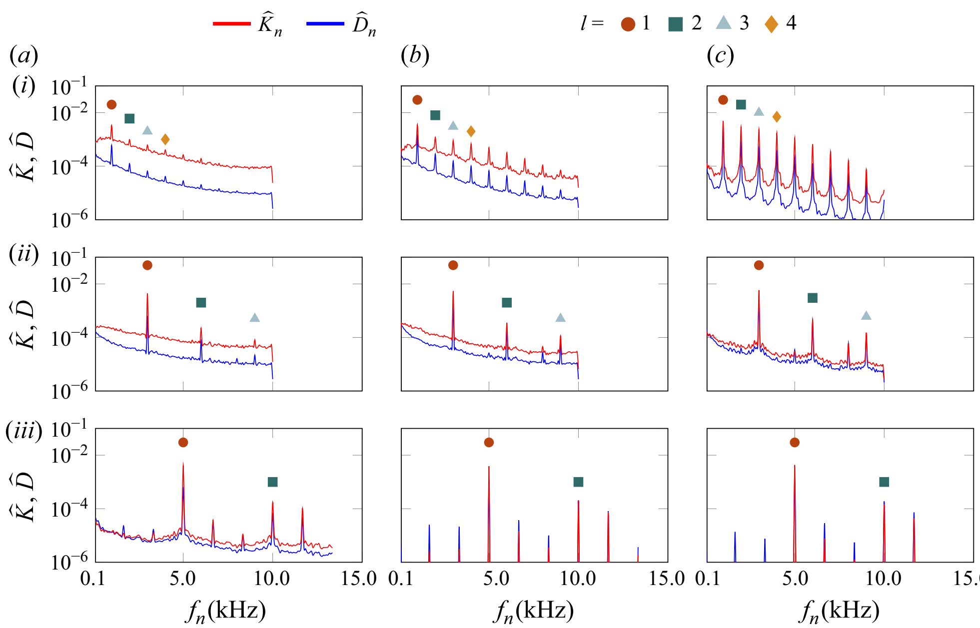

Figure 33. Viscous loss, $\widehat{D}_n$, and frequency-weighted KE spectra, $\widehat{K}_n$, for the complementary *St*–*Re* combinations at $ISPL = 150$ dB shown in figure 23. Cases in column (*a*)–(*c*) represent $Re = Re_0$, $Re_0/2$ and $Re_0/3$. Cases in row (*i*)–(*iii*) represent $St = 2St_0$, $6St_0$ and $10St_0$.

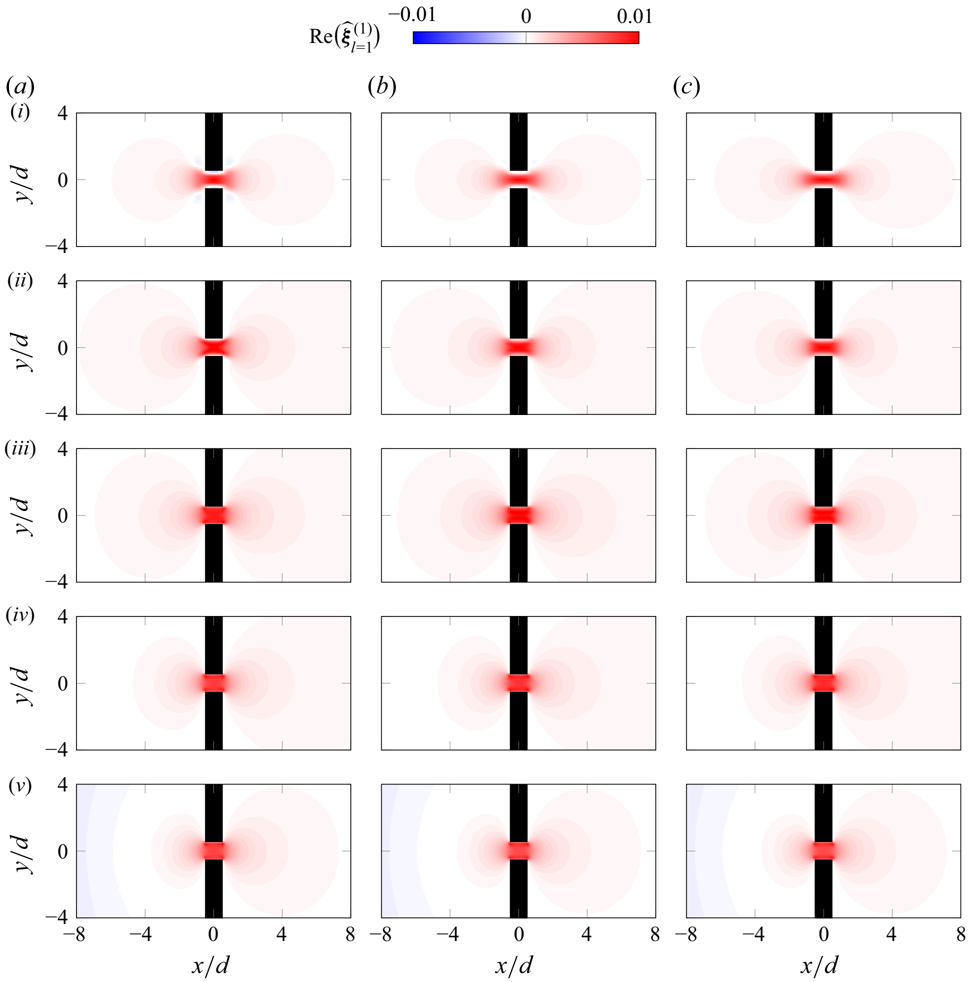

Figure 34. Leading SPOD modes, $\mathrm{Re}(\widehat{\boldsymbol{\xi}}^{(1)}_{l=1})$, for selected *St*–*Re* combinations at $ISPL = 120\,\mathrm{dB}$, plotted at their respective fundamental frequencies ($l = 1$) as their x-directional components, u. Cases in column (*a*)–(*c*) represent $Re = Re_0$, $Re_0/2$ and $Re_0/3$. Cases in row (*i*)–(*v*) represent $St = St_0$, $2St_0$, $4St_0$, $8St_0$ and $12St_0$.

contribution at both $ISPL = 150$ and $ISPL = 120\,\mathrm{dB}$ conditions. This result justifies the incompressible assumption made in § 3.1.

https://doi.org/10.1017/jfm.2026.11896 Published online by Cambridge University Press

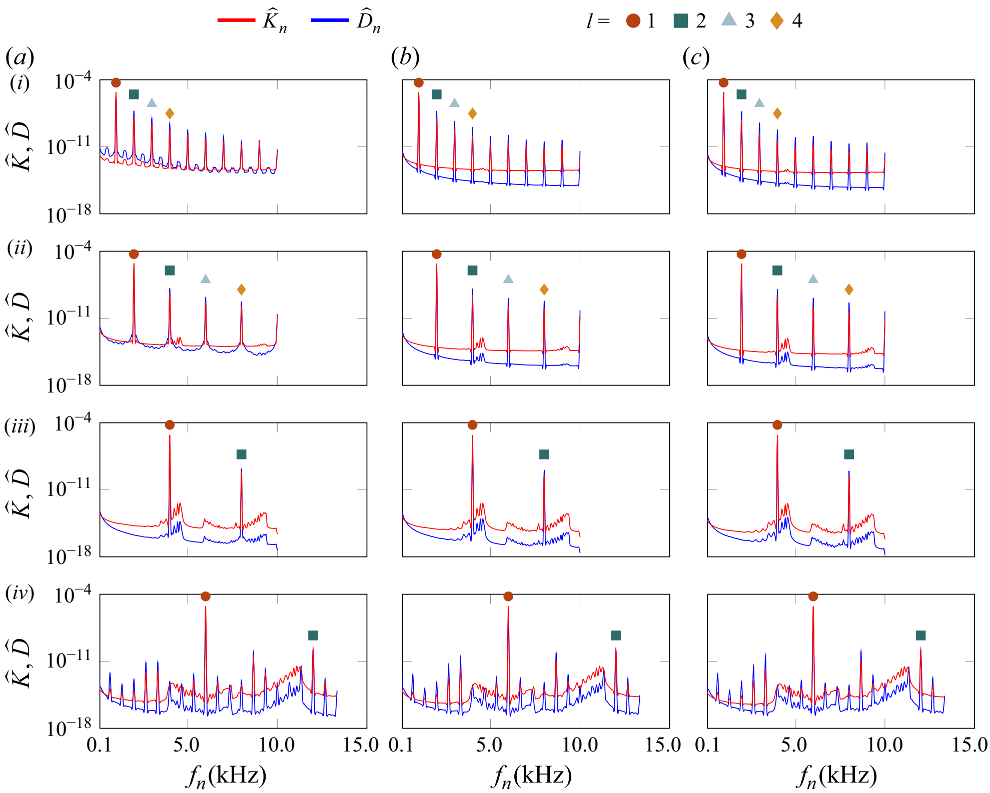

Figure 35. Viscous loss, $\widehat{D}_n$, and frequency-weighted KE spectra, $\widehat{K}_n$, for the complementary *St*–*Re* combinations at $ISPL = 120$ dB shown in figure 24. The fundamental frequency ($l = 1$ defined in (4.13)) and its higher-order harmonics ($l \geq 2$) are manifested as distinct peaks in the spectrum. Cases in column (*a*)–(*c*) represent $Re = Re_0$, $Re_0/2$ and $Re_0/3$. Cases in row (*i*)–(*iv*) represent $St = 2St_0$, $4St_0$, $8St_0$ and $12St_0$.

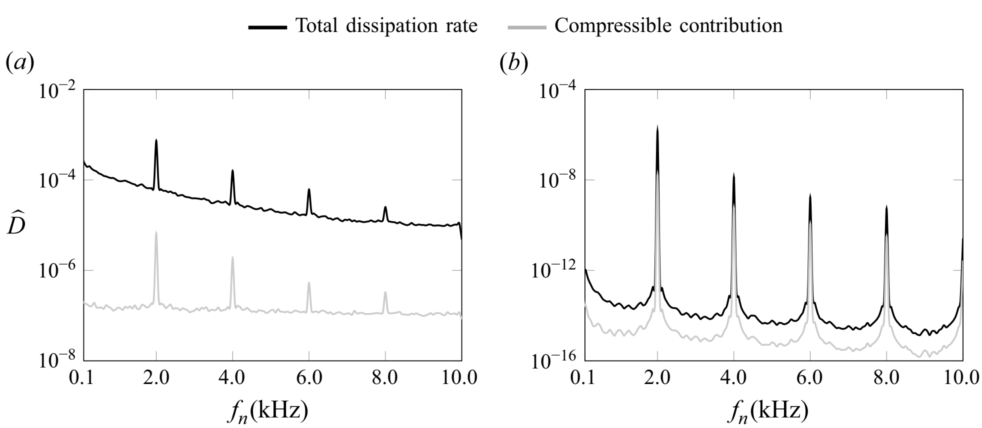

Figure 36. Total and compressible VL, $\widehat{D}_n$, contribution spectra at $St = 4St_0$ and $Re = Re_0$, subject to sound level at (*a*) $ISPL = 150$ dB and (*b*) $ISPL = 120$ dB. The compressible contributions are less than 1 % of the total viscous dissipation to justify the incompressible assumption in the spectral analysis.

REFERENCES

ABILY, T., REGNARD, J., GABARD, G. & DURAND, S. 2023 Non-linear effects in thin slits for low frequency sound absorption. *J. Sound Vib.* **546**, 117432.

AULITTO, A. 2023 Sound absorption mechanisms in perforated plates. PhD thesis, Eindhoven University of Technology.

AULITTO, A., HIRSCHBERG, A., ARTEAGA, I.L. & BUIJSSEN, E.L. 2022 Effect of slit length on linear and non-linear acoustic transfer impedance of a micro-slit plate. *Acta Acust.* **6**, 6.

AWASTHI, M., MCCRETON, S., MOREAU, D. & DOOLAN, C. 2025 Coherent oscillations and acoustic waves in a supersonic cylinder wake. *J. Fluid Mech.* **1012**, A27.

BERKOOZ, G., HOLMES, P. & LUMLEY, J.L. 1993 The proper orthogonal decomposition in the analysis of turbulent flows. *Annu. Rev. Fluid Mech.* **25**, 539–575.

BRYNGELSON, S.H., SCHMIDMAYER, K., CORALIC, V., MAEDA, K., MENG, J. & COLONIUS, T. 2021 MFC: an open-source high-order multi-component, multi-phase, and multi-scale compressible flow solver. *Comput. Phys. Commun.* **266**, 107396.

BUGEAT, B., KARBAN, U., AGARWAL, A., LESSHAFFT, L. & JORDAN, P. 2024 Acoustic resolvent analysis of turbulent jets. *Theor. Comput. Fluid Dyn.* **38**, 687–706.

CHEN, C. & LI, X. 2020 Microscopic fluid dynamics of a wire screen bound to a slit resonator excited by acoustic waves. *Phys. Fluids* **32** (11), 116107.

CHU, T. & SCHMIDT, O.T. 2025 Stochastic reduced-order Koopman model for turbulent flows. *Proc. R. Soc. Lond. A* **481**, 20250270.

CHUNG, J. & BLASER, D. 1980 Transfer function method of measuring in-duct acoustic properties. I. Theory. *J. Acoust. Soc. Am.* **68**, 907–913.

CORALIC, V. & COLONIUS, T. 2014 Finite-volume WENO scheme for viscous compressible multicomponent flows. *J. Comput. Phys.* **274**, 95–121.

CUMMINGS, A. 1984 Acoustic nonlinearities and power losses at orifices. *AIAA J.* **22**, 786–792.

FRANTZ, R.A.S., MIMEAU, C., SALIHOGLU, M., LOISEAU, J.-C. & ROBINET, J.-C. 2025 Bifurcation sequence in the wakes of a sphere and a cube. *J. Fluid Mech.* **1018**, A30.

GOTTLIEB, S. & SHU, C.-W. 1998 Total variation diminishing Runge–Kutta schemes. *Math. Comput.* **67**, 73–85.

HIMENO, F.H., SOUZA, D.S., AMARAL, F.R., RODRÍGUEZ, D. & MEDEIROS, M.A. 2021 SPOD analysis of noise-generating Rossiter modes in a slat with and without a bulb seal. *J. Fluid Mech.* **915**, A67.

HOPPEN, H., LANGFELDT, F., GLEINE, W. & VON ESTORFF, O. 2023 Helmholtz resonator with two resonance frequencies by coupling with a mechanical resonator. *J. Sound Vib.* **559**, 117747.

HOWE, M.S. 1980 The dissipation of sound at an edge. *J. Sound Vib.* **70**, 407–411.

INGARD, U. 1953 On the theory and design of acoustic resonators. *J. Acoust. Soc. Am.* **25**, 1037–1061.

INGARD, U. & LABATE, S. 1950 Acoustic circulation effects and the nonlinear impedance of orifices. *J. Acoust. Soc. Am.* **22**, 211–218.

KIDA, S. & ORSZAG, S.A. 1990 Energy and spectral dynamics in forced compressible turbulence. *J. Sci. Comput.* **5**, 85–125.

LANDAU, L.D. & LIFSHITZ, E.M. 1987 *Fluid Mechanics*, vol. 6. Elsevier.

LEUNG, R., SO, R., WANG, M. & LI, X. 2007 In-duct orifice and its effect on sound absorption. *J. Sound Vib.* **299**, 990–1004.

LUMLEY, J.L. 1967 The structure of inhomogeneous turbulent flows. In *Atmospheric Turbulence and Radio Wave Propagation*, pp. 166–178.

LUMLEY, J.L. 1970 *Stochastic Tools in Turbulence*. Academic Press.

MAEDA, K. & COLONIUS, T. 2017 A source term approach for generation of one-way acoustic waves in the Euler and Navier–Stokes equations. *Wave Motion* **75**, 36–49.

MELLING, T.H. 1973 The acoustic impedance of perforates at medium and high sound pressure levels. *J. Sound Vib.* **29**, 1–65.

MITTAL, R. & SEO, J.H. 2023 Origin and evolution of immersed boundary methods in computational fluid dynamics. *Phys. Rev. Fluids* **8**, 100501.

MIZUSHIMA, J. & HATSUDA, G. 2014 Nonlinear interactions between the two wakes behind a pair of square cylinders. *J. Fluid Mech.* **759**, 295–320.

NEKKANTI, A. & SCHMIDT, O.T. 2021*a* Modal analysis of acoustic directivity in turbulent jets. *AIAA J.* **59**, 228–239.

NEKKANTI, A. & SCHMIDT, O.T. 2021*b* Frequency–time analysis, low-rank reconstruction and denoising of turbulent flows using SPOD. *J. Fluid Mech.* **926**, A26.

NOGUEIRA, P.A.S., SELF, H.W.A., TOWNE, A. & EDGINGTON-MITCHELL, D. 2022 Wave-packet modulation in shock-containing jets. *Phys. Rev. Fluids* **7**, 074608.

Oosterhuis, J.P., Verbeek, A.A., Bühler, S., Wilcox, D. & van der Meer, T.H. 2017 Flow separation and turbulence in jet pumps for thermoacoustic applications. *Flow Turbul. Combust.* **98**, 311–326.

Qiang, X., Wang, P. & Liu, Y. 2022 Aeroacoustic simulation of transient vortex dynamics subjected to high-intensity acoustic waves. *Phys. Fluids* **34** (9), 093616.

Qu, R., Guo, J., Fang, Y., Zhong, S. & Zhang, X. 2023 Broadband quasi-perfect sound absorption by a metasurface with coupled resonators at both low-and high-amplitude excitations. *Mech. Syst. Signal Process.* **204**, 110782.

Radhakrishnan, A., Berre, H.L., Wilfong, B., Spratt, J.-S., Rodriguez, M., Jr, Colonius, T. & Bryngelson, S.H. 2024 Method for scalable and performant GPU-accelerated simulation of multiphase compressible flow. *Comput. Phys. Commun.* **302**, 109238.

Sano, A., Abreu, L.I., Cavalieri, A.V. & Wolf, W.R. 2019 Trailing-edge noise from the scattering of spanwise-coherent structures. *Phys. Rev. Fluids* **4**, 094602.

Sarpkaya, T. 1986 Force on a circular cylinder in viscous oscillatory flow at low Keulegan–Carpenter numbers. *J. Fluid Mech.* **165**, 61–71.

Scarano, F., Lyu, B., Paduano, A. & Avallone, F. 2026 Filtering acoustic from hydrodynamic velocity using modal decomposition methods on an acoustic liner under grazing turbulent flow. *J. Sound Vib.* **625**, 119568.

Schmid, P.J. 2010 Dynamic mode decomposition of numerical and experimental data. *J. Fluid Mech.* **656**, 5–28.

Schmidt, O.T. & Colonius, T. 2020 Guide to spectral proper orthogonal decomposition. *AIAA J.* **58**, 1023–1033.

Schmidt, O.T., Towne, A., Rigas, G., Colonius, T. & Brès, G.A. 2018 Spectral analysis of jet turbulence. *J. Fluid Mech.* **855**, 953–982.

Shuster, J.M. & Smith, D.R. 2007 Experimental study of the formation and scaling of a round synthetic jet. *Phys. Fluids* **19** (4), 045109.

Sirovich, L. 1987 Turbulence and the dynamics of coherent structures. I. Coherent structures. *Q. Appl. Maths* **45**, 561–571.

Tam, C.K., Ju, H., Jones, M.G., Watson, W.R. & Parrott, T.L. 2005 A computational and experimental study of slit resonators. *J. Sound Vib.* **284**, 947–984.

Tam, C.K., Ju, H., Jones, M.G., Watson, W.R. & Parrott, T.L. 2010 A computational and experimental study of resonators in three dimensions. *J. Sound Vib.* **329**, 5164–5193.

Tam, C.K., Ju, H. & Walker, B.E. 2008 Numerical simulation of a slit resonator in a grazing flow under acoustic excitation. *J. Sound Vib.* **313**, 449–471.

Tam, C.K. & Kurbatskii, K.A. 2000 Microfluid dynamics and acoustics of resonant liners. *AIAA J.* **38**, 1331–1339.

Tam, C.K., Kurbatskii, K.A., Ahuja, K. & Gaeta, R., Jr 2001 A numerical and experimental investigation of the dissipation mechanisms of resonant acoustic liners. *J. Sound Vib.* **245**, 545–557.

Tang, Y., Wang, P. & Liu, Y. 2023 A combined delayed detached eddy simulation and linearized Navier–Stokes equation study on the generation and reduction of aerodynamic noises inside steam turbine control valve with acoustic liner. *J. Fluids Engng* **145**, 121202.

Tang, Y., Wang, P. & Liu, Y. 2025 Phase-locking PIV measurement of vortex–vortex interactions inside dual-slit cavity during high-intensity acoustic modulation. *Exp. Therm. Fluid Sci.* **166**, 111483.

Thompson, K.W. 1990 Time-dependent boundary conditions for hyperbolic systems, II. *J. Comput. Phys.* **89**, 439–461.

Timmer, M.A., Oosterhuis, J.P., Bühler, S., Wilcox, D. & van der Meer, T.H. 2016 Characterization and reduction of flow separation in jet pumps for laminar oscillatory flows. *J. Acoust. Soc. Am.* **139**, 193–203.

Towne, A., Schmidt, O.T. & Colonius, T. 2018 Spectral proper orthogonal decomposition and its relationship to dynamic mode decomposition and resolvent analysis. *J. Fluid Mech.* **847**, 821–867.

Tseng, Y.-H. & Ferziger, J.H. 2003 A ghost-cell immersed boundary method for flow in complex geometry. *J. Comput. Phys.* **192**, 593–623.

Wang, J., Yang, Y., Shi, Y., Xiao, Z., He, X. & Chen, S. 2013 Cascade of kinetic energy in three-dimensional compressible turbulence. *Phys. Rev. Lett.* **110**, 214505.

Welch, P. 1967 The use of fast Fourier transform for the estimation of power spectra: a method based on time averaging over short, modified periodograms. *IEEE Trans. Audio Electroacoust.* **15**, 70–73.

White, F. 1991 *Viscous Fluid Flow*, 2nd edn. McGraw-Hill.

Wilfong, B., *et al.* 2025*a* MFC 5.0: an exascale many-physics flow solver. arXiv: 2503.07953.

WILFONG, B., *et al.* 2025*c* Simulating many-engine spacecraft: exceeding 1 quadrillion degrees of freedom via information geometric regularization. In *SC25*, pp. 14–24. ACM.

WILFONG, B., RADHAKRISHNAN, A., BERRE, H.A.L., PRATHI, T., ABBOTT, S. & BRYNGELSON, S.H. 2025*b* Testing and benchmarking emerging supercomputers via the MFC flow solver. In *SC25 Workshops*, pp. 669–677. ACM.

WOMERSLEY, J.R. 1955 Method for the calculation of velocity, rate of flow and viscous drag in arteries when the pressure gradient is known. *J. Physiol.* **127**, 553.

XU, J., LI, X. & GUO, Y. 2014 Nonlinear absorption characteristic of micro resonator under high sound pressure level. In *20th AIAA/CEAS Aeroacoustics Conference*, *AIAA Paper* 2014-3353. American Institute of Aeronautics and Astronautics.

YEUNG, B., CHU, T. & SCHMIDT, O.T. 2026 Triadic orthogonal decomposition reveals nonlinearity in fluid flows. *J. Fluid Mech.* **1031**, A34.

YU, H., AHUJA, K.K., SANKAR, L.N. & BRYNGELSON, S.H. 2024 Numerical investigation of leakage of high-amplitude sound in ill-fitting earplugs. In *AIAA AVIATION*, p. 4391. American Institute of Aeronautics and Astronautics.

YU, H., AHUJA, K.K., SANKAR, L.N. & BRYNGELSON, S.H. 2025*a* Transmission of high-amplitude sound through leakages of ill-fitting earplugs. arXiv: 2510.16355.

YU, H., CHU, T. & BRYNGELSON, S.H. 2025*b* Direction numerical simulation data: 2D acoustic slit.. Available at: https://doi.org/10.35090/gatech/80504.

ZHANG, Q. & BODONY, D.J. 2011 Numerical simulation of two-dimensional acoustic liners with high-speed grazing flow. *AIAA J.* **49**, 365–382.

ZHANG, Q. & BODONY, D.J. 2016 Numerical investigation of a honeycomb liner grazed by laminar and turbulent boundary layers. *J. Fluid Mech.* **792**, 936–980.